



Report 3 on the PARIS Calorimeter Simulations

*IPN Lyon, 69622 Villeurbanne, France
October 2007*

Segmentation

Abstract

This work is a continuation of the study reported in [1, 2] on the simulations for the PARIS calorimeter. Presently, we investigate possible segmentation of the array.

As starting point for the study of segmentation, let us consider the following test case. The geometry consists of an ensemble of two complete concentric spherical layers, which are supposed to be constituted of perfectly placed side by side segments (no hole). The size of the segments is defined by a uniform cutting according to either ϑ and ϕ or $\cos\vartheta$ and ϕ . The generator consists of a cascade with a single γ -ray. 250,000 photons are shoot. This simplified scheme enables performing a detailed study of the pattern of fired segments around the incident hit and of the associated energy deposit in each segment. This pattern, which critically depends on the incident γ -ray energy, will be further used for determining how hits and energy deposits shall be packed and add-backed to restore the initial true particle energy, multiplicity and direction.

The solid angle subtended by a segment depends upon the number of desired segments, of course, but also on the coordinate space in which segmentation is made. While a uniform cutting according to (ϑ, ϕ) does not lead to identical solid angles for each individual segment, a uniform segmentation wrt to $(\cos\vartheta, \phi)$ does (although the segments are not identical in shape). To illustrate this point, the angles (ϑ, ϕ) as well as the solid angle subtended by each cell are shown in Figure 22. A uniform cutting made of 15 segments according to ϑ (1st row) or to $\cos\vartheta$ (2nd row) is considered for $0^\circ < \vartheta < 180^\circ$. In both cases, 15 segments uniformly spaced are assumed along the ϕ direction with $-180^\circ < \phi < 180^\circ$. Each cell is numbered with the subscripts i and j referring to the ϑ and ϕ coordinates, respectively (i and j run from 1 to 15 presently). For a uniform segmentation along ϑ and ϕ , the solid angle Ω subtended by a given cell is not constant but depends on ϑ . On the contrary, for a uniform segmentation along $\cos\vartheta$ and ϕ , all cells located at a given distance from the source are characterized by the same Ω but the ϑ angles they subtend are not equal. Both options are provided in the PARIS package. The suited segmentation might be somewhere in between these two configurations.

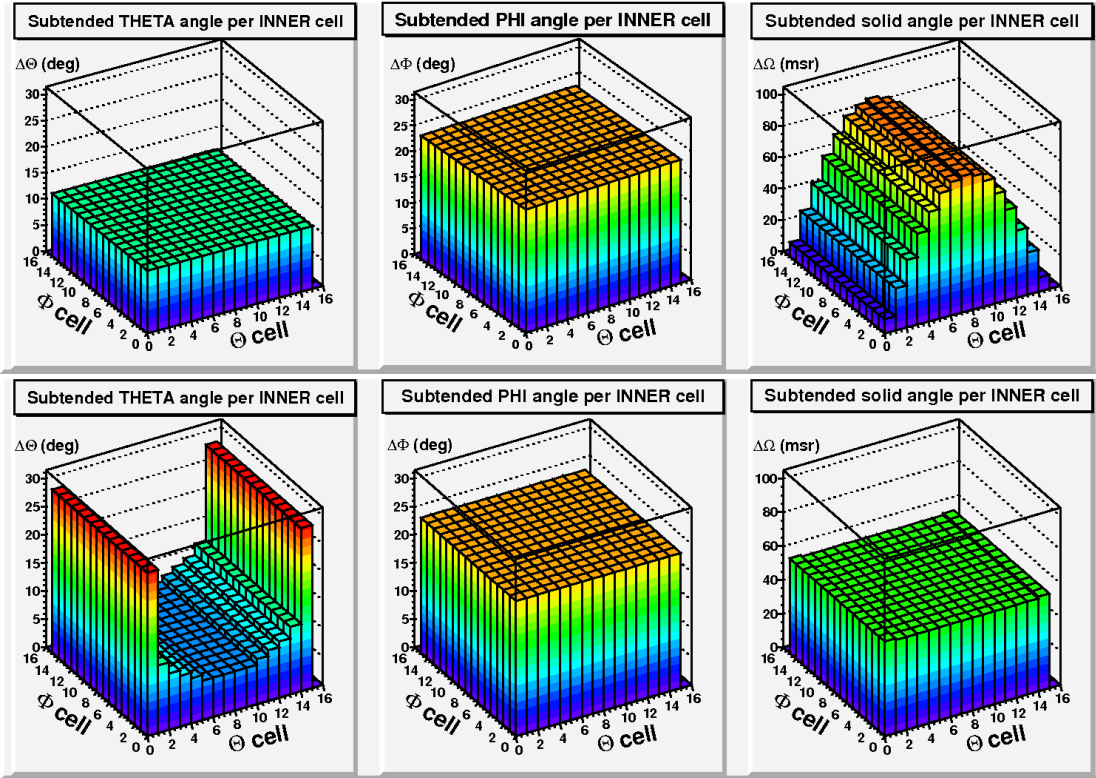


Fig. 22: Angles (ϑ, ϕ, Ω) subtended by each cell of a 15×15 matrix for a spherical geometry, see the text. Provided the segmentation in both layers is the same, the angles subtended by the inner and outer shell are, of course, identical. The first row corresponds to uniform cutting along ϑ and ϕ , whereas the second row refers to uniform cutting along $\cos\vartheta$ and ϕ . The distance from the source is 10cm.

The observables we will concentrate on first are :

- the fold F_γ , defined as the number of cells fired (one fold defined per shell),
- the pattern of fired cells around the incident direction,
- the individual energy deposited in each fired cell,
- the percentage of energy absorbed per cell,
- the absorption efficiency per cell.

These quantities are studied for both the inner and outer shells, independently. Yet, we shall keep in mind that the information from the 2 shells has to be combined, namely in terms of number of counts (e.g. what is absorbed in the inner shell is not seen by the outer shell). Various incident energies and different segmentations are investigated. A cell is assumed to be fired as soon as a non zero energy deposit is observed there (no threshold consideration).

1. Fold and pattern of the fired cells

Figures 23-26 display some of the aforementioned quantities for an inner 5cm thick LaBr_3 (with $R_{\text{in}}=10\text{cm}$ and $R_{\text{out}}=15\text{cm}$) coupled to an outer 15cm thick CsI layer (with $R_{\text{in}}=30\text{cm}$ and $R_{\text{out}}=45\text{cm}$). The segmentation is taken identical in both shells and assumed uniform in ϑ and ϕ with 15 cells in both directions. The ϑ interval subtended by successive segments are 12° broad while ϕ intervals are 24° wide. The precise limiting values of the angles subtended by each cell are given in Appendix A, Table 1. With such a segmentation, the solid angles

subtended by the cells are *not* identical (see Fig.22). The direction of the incident γ -ray points at $(\vartheta, \phi) = (90^\circ, 0^\circ)$.

The number of fired inner and outer cells is shown in Fig.23 for various incident energies E_{inc} . The mean value of F_γ as well as the variance extracted from these distributions are drawn as function of E_{inc} in Fig.24. The number of cells fired first steadily increases in the inner shell with increasing E_{inc} up to a few MeV. This is caused by the dominance of Compton scattering which extends more and more with increasing E_{inc} [1]. Above a few MeV, the onset of pair creation in the inner shell (leading to more focused showers), on one side, combined to the larger probability for scattered particles to reach the outer shell after interaction in the inner shell and to the larger probability for transparency of the inner shell, on the other side, leads to a fold in the inner shell which does not increase strongly while the fold in the outer layer progresses rather fast. Transparency of the inner layer is recognizable by the peak at zero fold. At the highest energies, nonetheless, the inner fold extends further, most probably because of the large amount of more and more scattered secondary particles. The latter also explain the increase of the outer fold. Analysis of mean values of the fold (such as in Fig.24) has to be taken with caution due to the potential double-humped nature of the fold distribution.

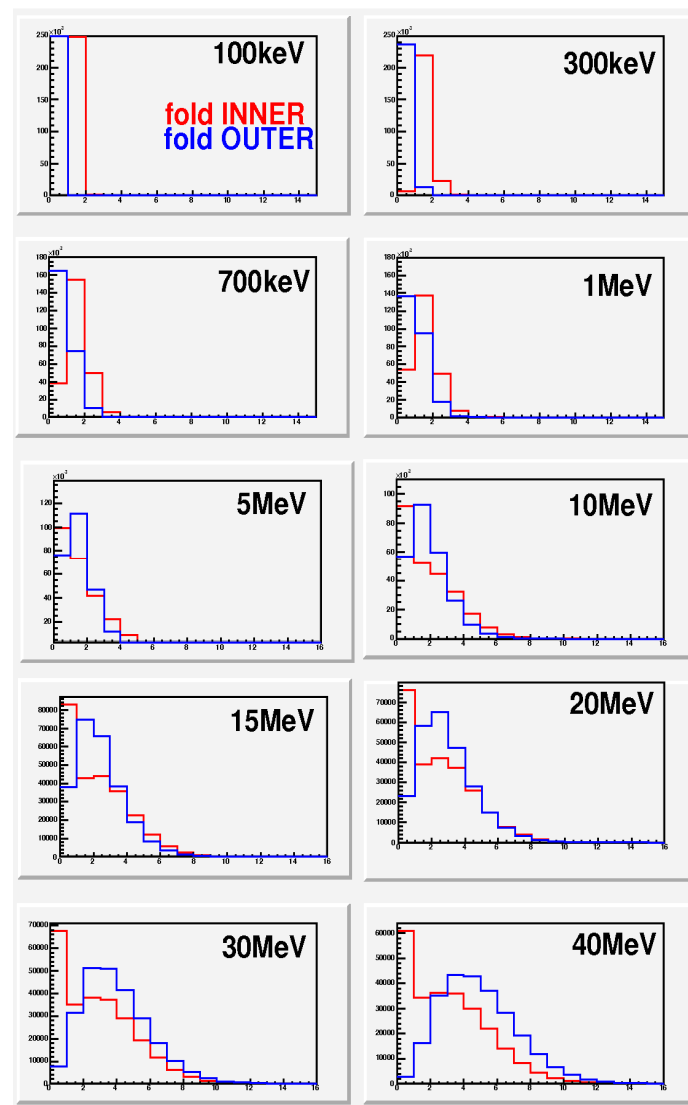


Fig. 23: Distribution of the number of fired cells in the inner (red) and outer (blue) layer for various incident energies and a two-shell geometry (inner LaBr3 layer - $R_{in}=10\text{cm}$, $R_{out}=15\text{cm}$ + outer CsI layer - $R_{in}=20\text{cm}$, $R_{out}=35\text{cm}$). Segmentation is taken uniform in ϑ and ϕ , see the text.

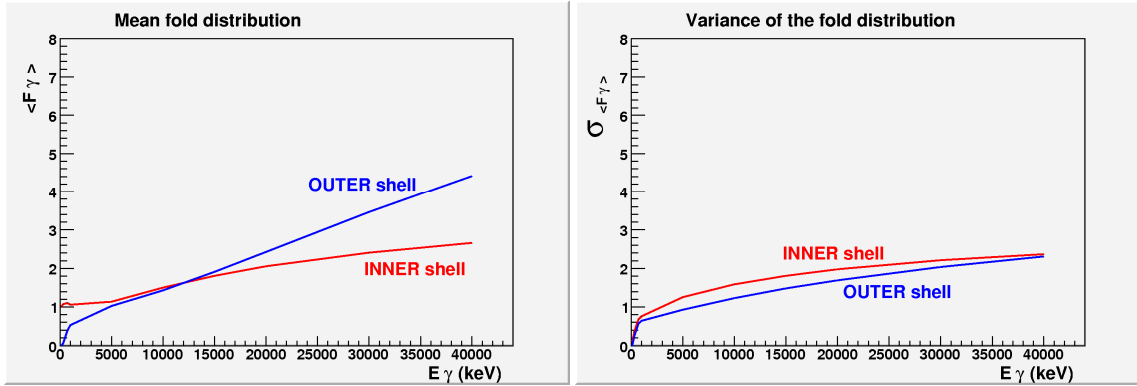


Fig. 24: Left: Mean fold $\langle F_\gamma \rangle$ as function of incident energy for the inner (red) and outer (blue) shell. Right: Variance of the F_γ distribution as function of incident energy for the inner (red) and outer (blue) shell. Segmentation is taken uniform in ϑ and ϕ , see the text.

In order to investigate in detail the pattern of the fired cells around the direction of the incident particle, Figures 25 and 26 display the correlations between the hit cells along the ϑ and ϕ directions as obtained under various circumstances. Namely, gates have – or have not – been applied to the shell which is fired first in the event. Also, each impact has – or not – been weighted with the percentage of energy deposited at the corresponding impact point (see [1]). Note that the incident particle exactly points at the centre of cells (7,7).

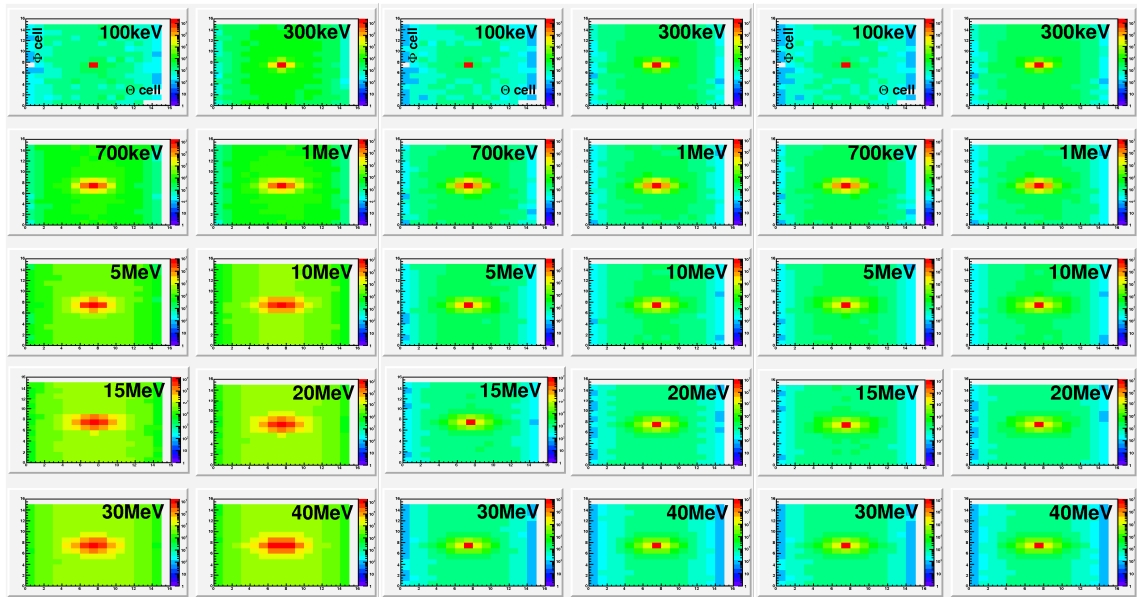


Fig. 25: Correlation between the subscripts of the inner hit cells in ϑ (x-axis) and ϕ (y-axis) direction. All impacts generated by the single incident γ contribute. The left and middle panels consider only those events for which the inner shell fired first, while the right most picture includes all events. For the leftmost panel, all impacts have the same weight, whereas weighting wrt the energy deposit is applied for the middle and right panels. Note the logarithmic z-scale.

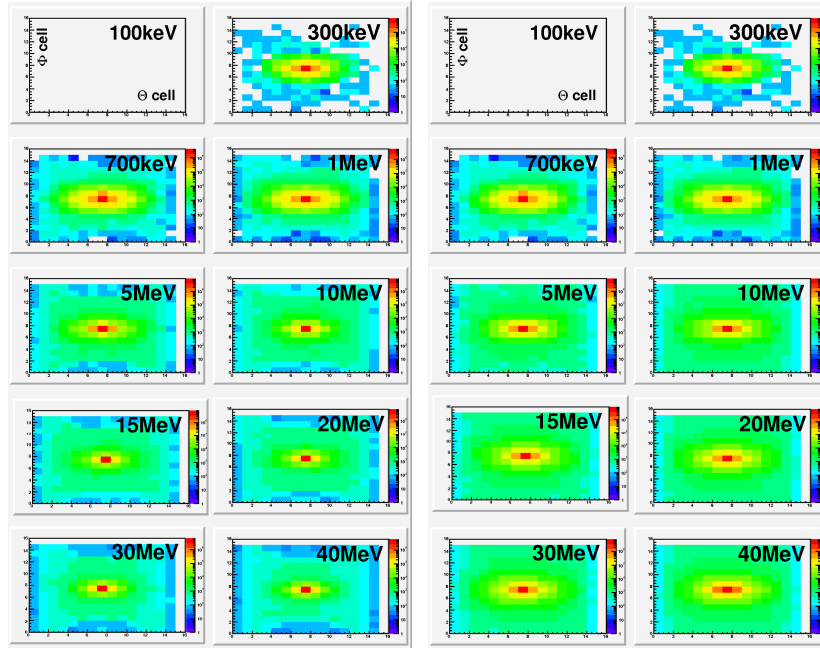


Fig. 26: Correlation between the subscripts of the outer hit cells in ϑ and ϕ direction. All impacts generated by a single incident γ contribute. The left panel considers only those events for which the outer shell fired first, while the right picture includes all events. For both panels, weighting wrt the energy deposit is considered.

It is obvious from Fig.25 (left-most and middle panels) that the information on the amount of energy deposited in a given cell is strongly related to the sequence of the fired cells. Thus, this information is very helpful along the determination of the most probable direction of the incident particle and the location of the first interaction hit. This feature will be studied in detail in section 2. The correlation pattern of the fired cells corroborates the discussion made in [1] about the angular extension of the shower generated by an incident γ -ray of given energy. The fact that the patterns are not symmetric in (ϑ, ϕ) is due to wider cells along ϕ , what implies a greater number of fired cells along the x -axis. For the inner shell, the spectra with and without gating on the shell which is fired first are very similar. That is in line with the small probability for retro-diffusion from the outer to the inner shell. Conversely, for the outer shell (see Fig.26), the spectra restricted to events which interact first in the outer shell present a much smaller number of fired cells than in the case first interaction takes place in the inner shell. This observation again is in line with what concluded in [1, 2] about the dependence of the size of the shower in the outer shell on its size in the inner layer.

The quantities displayed in Figures 23-26 for a uniform segmentation along ϑ and ϕ are shown in Figures 27-30 for a 15×15 segmentation uniform along $\cos\vartheta$ and ϕ . In this case, the ϕ interval covered by all cells is 24° wide as previously, whereas the ϑ angle subtended by successive segments is not constant. The precise limiting values of the angles of each cell are given in Appendix A, Table 2. With such a segmentation, the solid angles subtended by the cells are all identical (see Fig.22). A slight increase of the fold is observed for both shells. The hit cell patterns reveal that this increase has to be ascribed to the greater number of fired cells in ϑ direction. That is readily understood by the finer segmentation achieved via a $\cos\vartheta$

cutting near the present direction ($90^\circ, 0^\circ$) of the incident γ (cf. Appendix A). The dependence on the direction of the incoming particle situation will be studied further below.

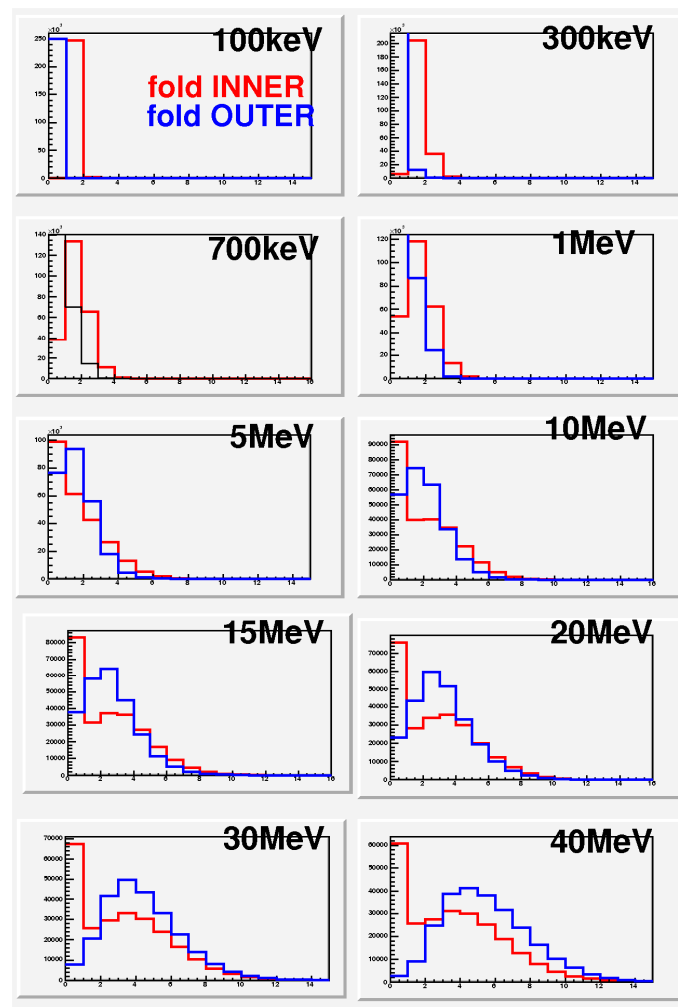


Fig. 27: Distribution of the number of fired cells in the inner (red) and outer (blue) layer for various incident energies and a two-shell geometry (inner LaBr3 layer - $R_{in}=10\text{cm}$, $R_{out}=15\text{cm}$ + outer CsI layer - $R_{in}=20\text{cm}$, $R_{out}=35\text{cm}$). Segmentation is taken uniform in $\cos\vartheta$ and ϕ , see the text.

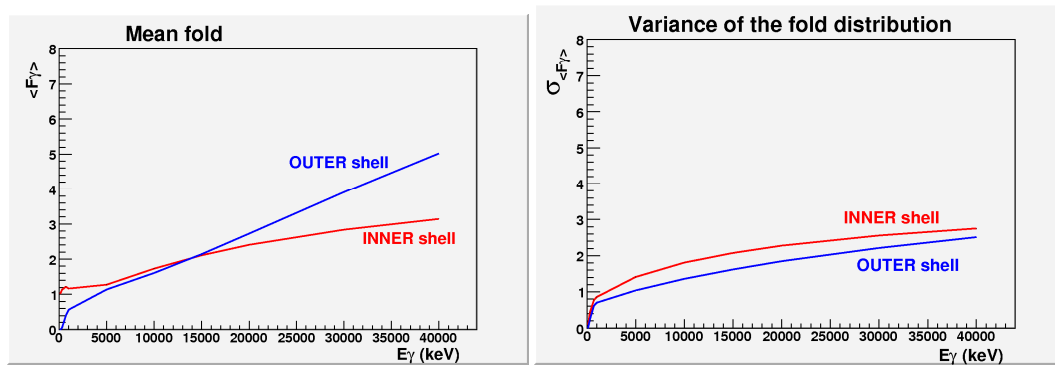


Fig. 28: Left: Mean fold $\langle F_\gamma \rangle$ as function of incident energy for the inner (red) and outer (blue) shell. Right: Variance of the F_γ distribution as function of incident energy for the inner (red) and outer (blue) shell. Segmentation is taken uniform in $\cos\vartheta$ and ϕ , see the text

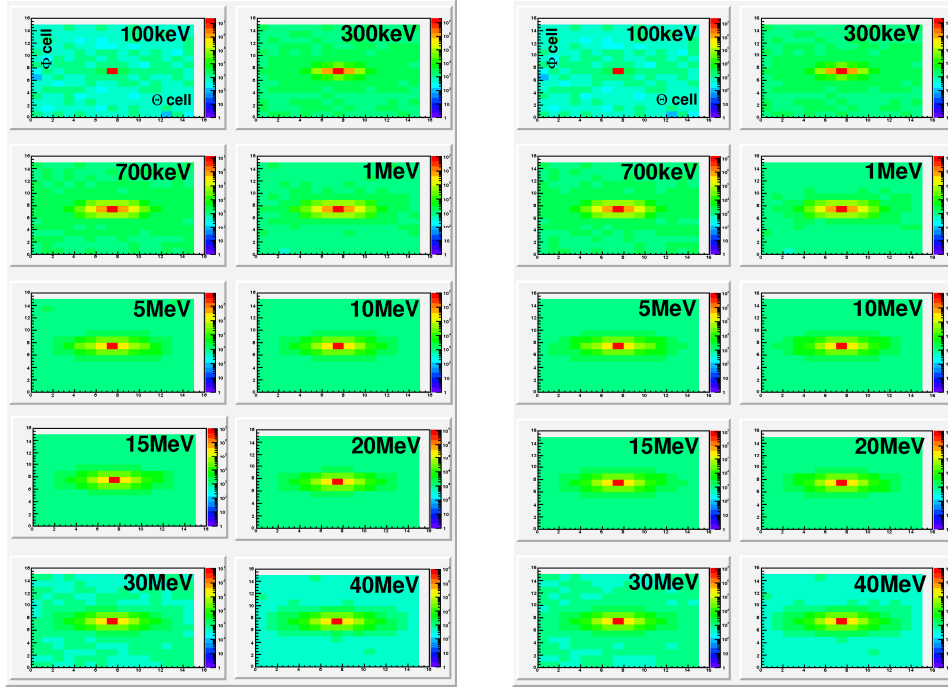


Fig. 29: Correlation between the subscripts of the inner hit cells in ϑ (x -axis) and ϕ (y -axis) direction. All impacts generated by the single incident γ contribute. The left panel considers only those events for which the inner shell fired first, while the right picture includes all events. In both cases, weighting wrt the energy deposit is applied. Segmentation is taken uniform in $\cos\vartheta$ and ϕ , see the text.

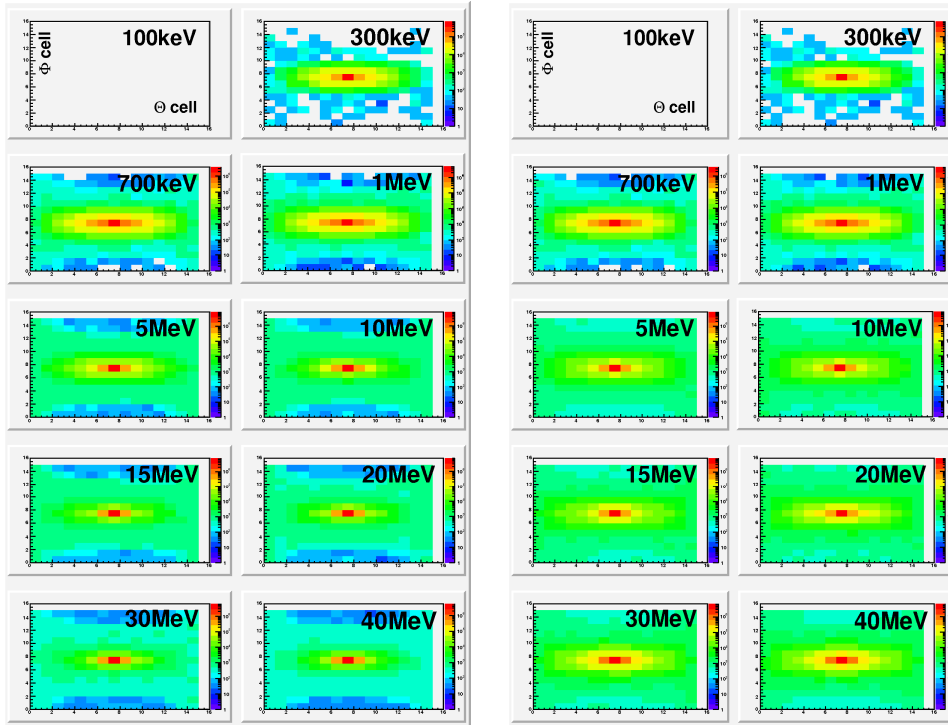


Fig. 30: Correlation between the subscripts of the outer hit cells in ϑ (x -axis) and ϕ (y -axis) direction. All impacts generated by the single incident γ contribute. The left panel considers only those events for which the

outer shell fired first, while the right picture includes all events. In both cases, weighting wrt the energy deposit is applied. Segmentation is taken uniform in $\cos\vartheta$ and ϕ , see the text.

Note that for the outer layer the end-caps of the spherical layer ($\vartheta \sim 0^\circ$ and $\vartheta \sim 180^\circ$) are more uniformly populated along ϕ as compared to more central ϑ crowns, in comparison with the inner layer. This might be related to the much thicker second shell (15cm of CsI) as compared to the thin inner shell (5cm of LaBr3) for similar densities. The probability for secondary particles to explore the full space is higher. This seems to be corroborated by the results displayed in Fig.30' where two CsI outer shell thickness are compared. Also, the effect is more pronounced for a uniform segmentation along $(\cos\vartheta, \phi)$ than along (ϑ, ϕ) , most probably because of the larger solid angle subtended by the end-caps in the former case.

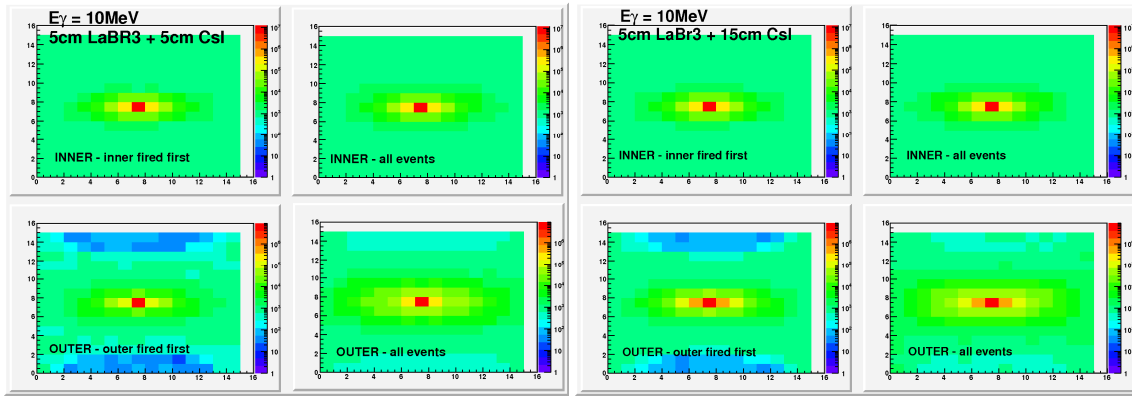


Fig. 30': Correlation between the subscripts of the inner (first rows) and outer (second rows) hit cells in ϑ (x -axis) and ϕ (y -axis) direction. The left panels corresponds to the assembly (5cm LaBr3 + 5cm CsI) and the right panel to (5cm LaBr3 + 15cm CsI). In each panel the leftmost column considers only those events for which the inner or outer shell fired first, while the right picture includes all events. A photon incident energy of 10MeV is considered only.

The influence of the number of segments of the array on fold and hit pattern is investigated in Fig.31-32 and Fig.33-34 for a 9×9 (9 cells in $\cos\vartheta$ and ϕ directions) and a 9×15 (9 cells along $\cos\vartheta$ and 15 along ϕ) segmentation, respectively. We restrict here to uniform cutting according to $\cos\vartheta$ and ϕ , which might constitute the simplest case in first stage since all segments subtend the same solid angle. Note in the figures that the range covered by the display depends on the total number of cells (up to either 10 or 16). As expected, the fold as well as the pattern of fired cells are directly related to the mesh of the segmentation. The finer the segmentation, the larger the number of fired cells. Yet, as far as ϕ is concerned, the picture is nearly identical for the 9×9 and 15×15 segmentations, since a 24° aperture nearly matches the angular extension of the shower [1]. As for the 15×15 case, the large spread of the hit cells in the outer shell is mostly caused by events which first interaction takes place in the inner shell. A minimum of 9 segments along either $\cos\vartheta$ or ϑ and 15 segments along ϕ is probably mandatory; at the price of a too much worse angular resolution. Nonetheless, further more quantitative investigations are required to settle this point.

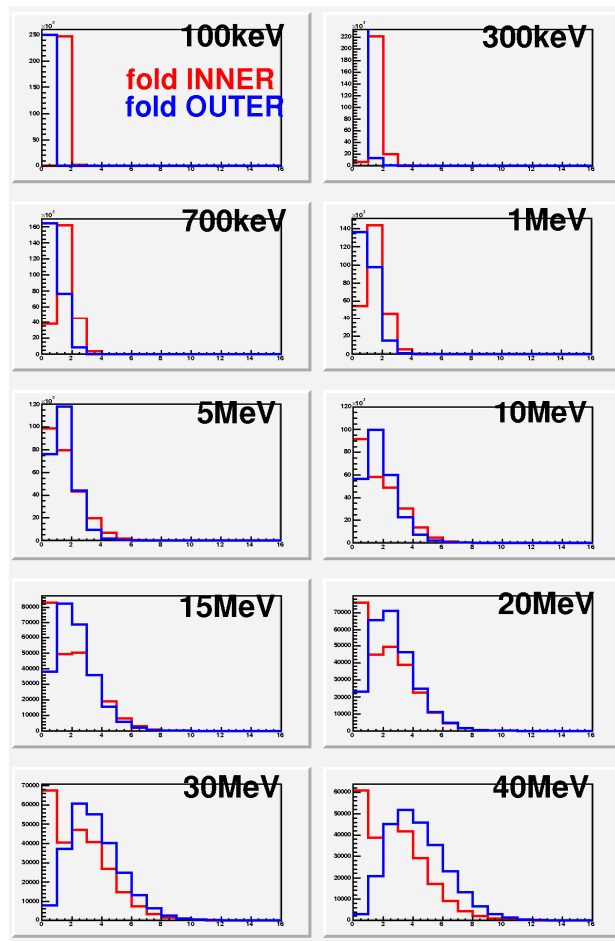


Fig. 31: Identical to Fig.27 for a 9×9 segmentation taken uniform in $\cos\theta$ and ϕ , see the text.

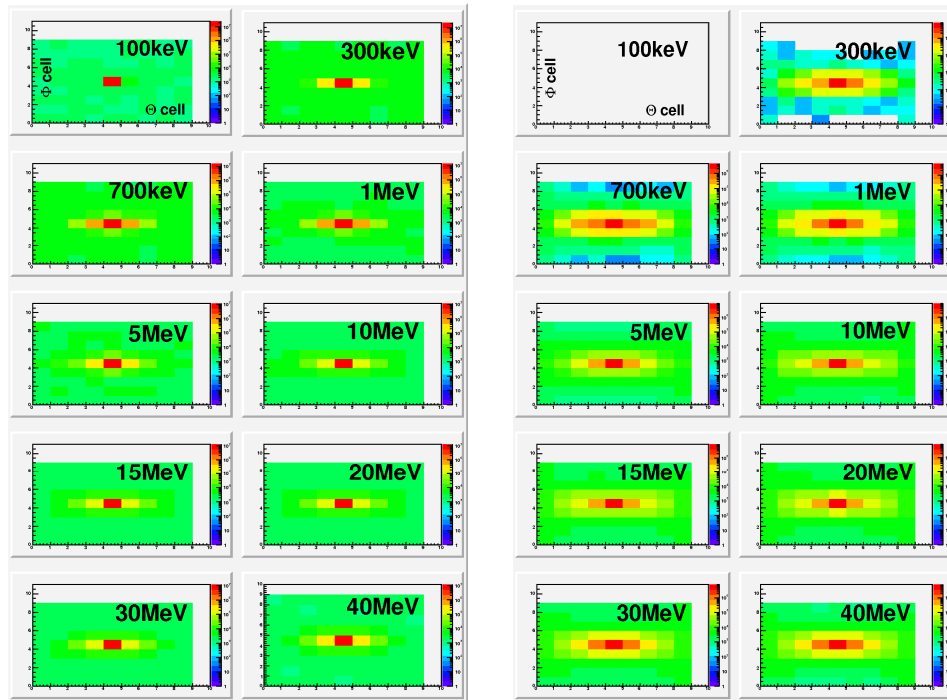


Fig. 32: Left: Correlation between the inner hit cells in ϑ (x -axis) and ϕ (y -axis) direction. Right: Correlation between the outer hit cells in ϑ (x -axis) and ϕ (y -axis) direction. All impacts generated by the single incident γ contribute. All events are included, independently on the shell which is fired first, and weighting wrt the energy deposit is applied. The segmentation is of 9×9 kind and taken uniform in $\cos\vartheta$ and ϕ , see the text.

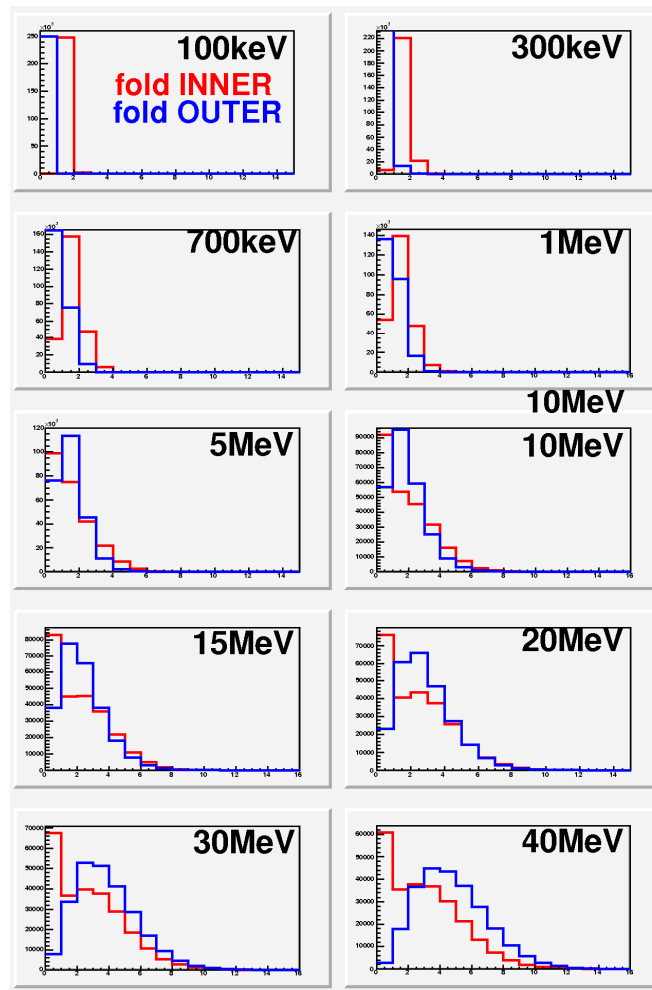


Fig. 33: Identical to Fig.27 for a 9×15 segmentation taken uniform in $\cos\vartheta$ and ϕ , see the text.

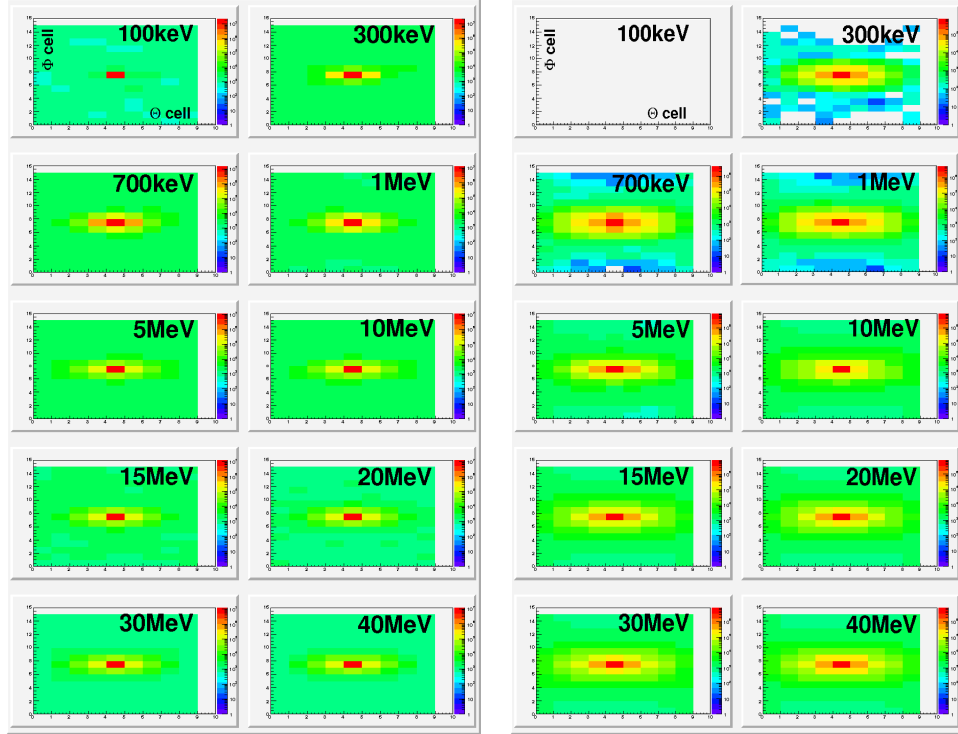


Fig. 34: Identical to Fig.32 for a 9×15 segmentation is taken uniform in $\cos\vartheta$ and ϕ , see the text.

How the direction of the incoming particle modifies the above observations is studied in Fig.35-36 where the incident γ -ray direction points at $(45^\circ, 0^\circ)$ instead of $(90^\circ, 0^\circ)$. A 15×15 segmentation uniformly distributed along $\cos\vartheta$ and ϕ is assumed. The number of fired cells is very slightly larger than what obtained for $(90^\circ, 0^\circ)$ due to the smaller ϑ angle subtended by the cell around 45° as compared to 90° (cf. Table 2 of Appendix A). The pattern of the fired cell looks very similar and is basically shifted towards smaller ϑ -indexes. To highlight more ‘tricky’ geometrical effects, we show in Fig.37 the folds and hit patterns for an incident 5MeV γ -ray pointing at $(0^\circ, 0^\circ)$: for ϑ and ϕ strictly equal to zero, all ϕ cells of a crown are equiprobable. Thus, all cells are fired along ϕ , leading to a dramatic increase of folds. Fortunately, this peculiar case is excluded by experimental constrains (beam pipe namely).

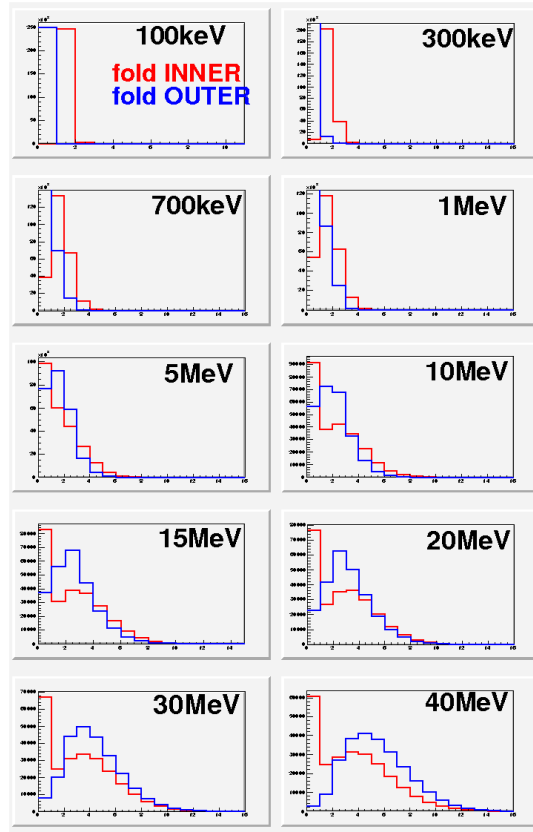


Fig. 35: Identical to Fig.27 for a 15×15 segmentation taken uniform in $\cos\vartheta$ and ϕ , but with the incident particle pointing at $(45^\circ, 0^\circ)$ instead of $(90^\circ, 0^\circ)$.

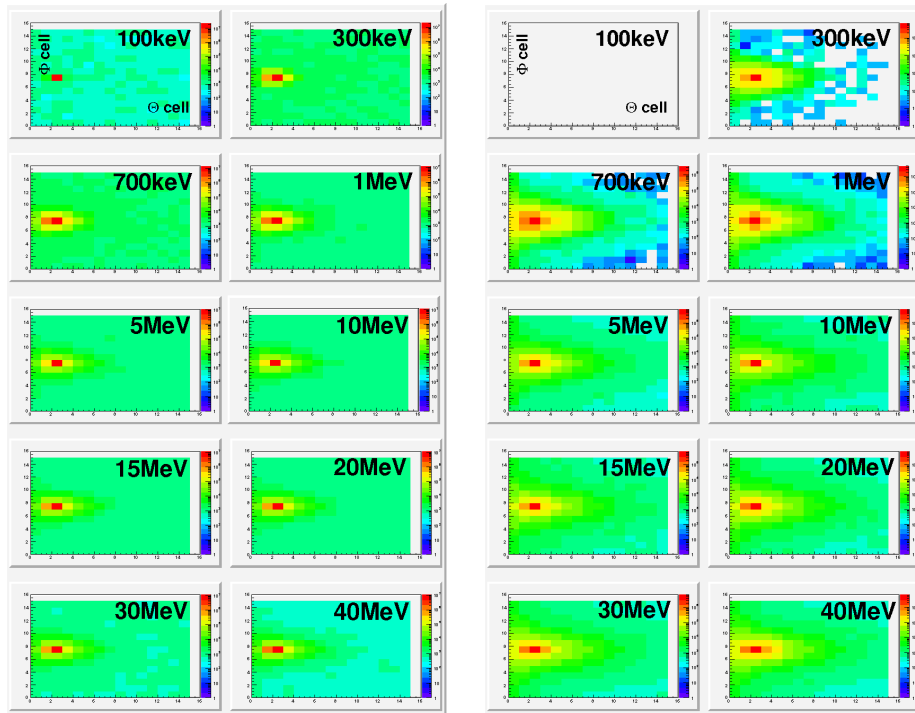


Fig. 36: Left: Correlation between the inner hit cells in ϑ (x -axis) and ϕ (y -axis) direction. Right: Correlation between the outer hit cells in ϑ (x -axis) and ϕ (y -axis) direction. All impacts generated by the single incident γ

contribute. All events are included, independently on the shell which is fired first, and weighting wrt the energy deposit is applied. The segmentation is of 15×15 kind and taken uniform in $\cos\vartheta$ and ϕ , see the text. In contrast to previously, the incident particle pointing at $(45^\circ, 0^\circ)$ instead of $(90^\circ, 0^\circ)$.

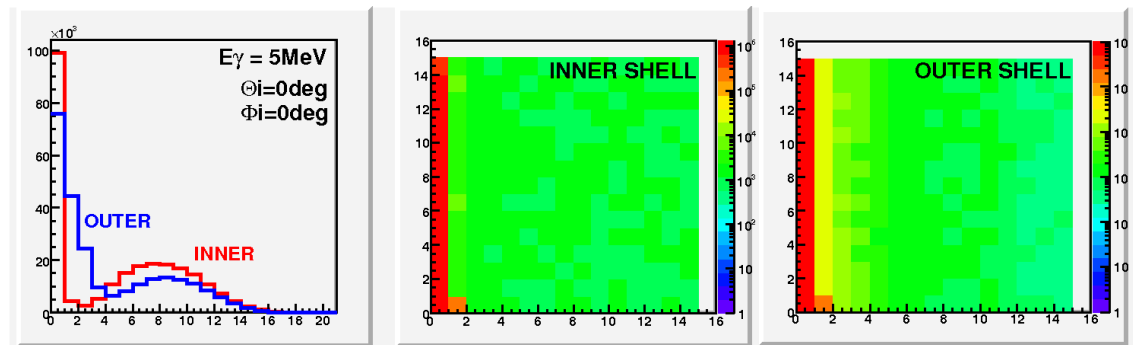


Fig. 37: Leftmost panel : Identical to Fig.27 for a 5MeV incident photon pointing at $(0^\circ, 0^\circ)$. Central and rightmost panels: Identical to Fig.36 for an incident particle pointing at $(0^\circ, 0^\circ)$.

A more detailed study of the influence of the incident direction of the incoming particle is given in Fig.38-40 for a γ -ray of 5MeV energy. The fold and hit pattern are compared for various incident ϑ and ϕ angles. In Fig.38 and 39, ϕ is fixed at 0° . Conversely, for Fig.40, ϑ is constant and set at 45° while ϕ is varying. For angles not too much close to 0° , the fold distribution does not sizeably depend on the ϑ of the incoming photon. The pattern of the fired cells does slightly only. There is no dependence on ϕ and the patterns of Fig.40 are simply shifted according to the ϕ -index of the incident direction. The increase of the number of hit cells for $\phi=180^\circ$ is due to the fact that, at variance with $\phi=0^\circ, 45^\circ, 90^\circ, 230^\circ$, $\phi=180^\circ$ corresponds exactly to the frontier between two cells. Note also that, along varying either ϑ or ϕ , additional differences are caused by the fact that the chosen incident direction is more or less close to the centre of a given cell.

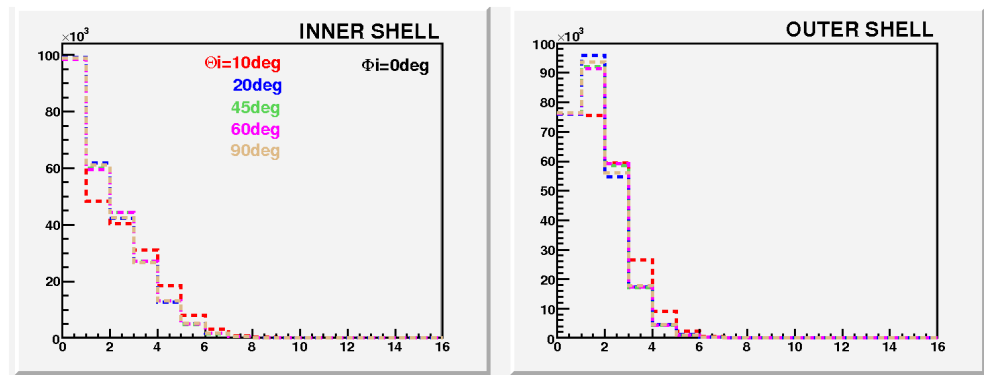


Fig. 38: Distribution of the number of fired cells in the inner (left) and outer (right) shell for an incident 5MeV energy and various incident ϑ angles as indicated, see the text. Segmentation is assumed uniform in $\cos\vartheta$ and ϕ .

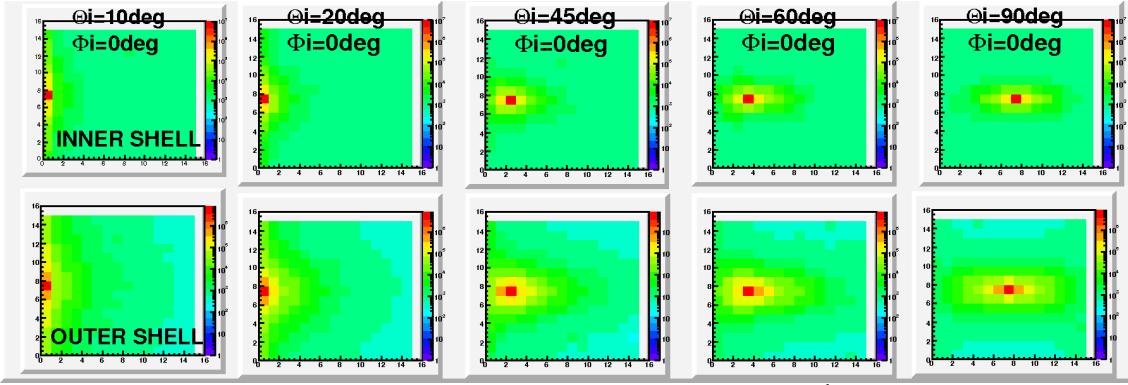


Fig. 39: 1st row: Correlation between the inner hit cells in ϑ and ϕ direction. 2nd row: Correlation between the outer hit cells in ϑ and ϕ direction. In both rows, an incident photon of 5MeV energy is considered. Each column correspond to another incident ϑ angle, as indicated, while ϕ is set at 0° .

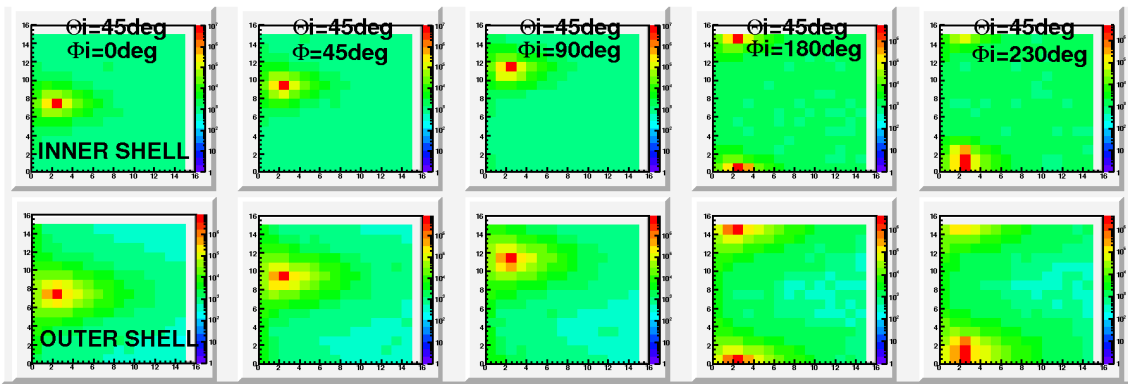


Fig. 40: 1st row: Correlation between the inner hit cells in ϑ and ϕ direction. 2nd row: Correlation between the outer hit cells in ϑ and ϕ direction. In both rows, an incident photon of 5MeV energy is considered. Each column correspond to another incident ϕ angle, as indicated, while ϑ is set at 45° .

For the configuration of a uniform segmentation along $(\cos\vartheta, \phi)$ – i.e. same solid angle for all cells - the above observations imply a reconstruction which may depend on ϑ , in addition to its dependence on the photon energy. This problem can be solved to some extent via a segmentation which is *not* uniform by using segments of different size and shape. A less fine segmentation at small angles would make similar the energy deposit and multiplicity pattern to those obtained at large angles. That could yield a single reconstruction algorithm suited for the whole array. However, at the same time, a gross segmentation deteriorates the angle determination and, thus, the Doppler correction most critical at small angles. A compromise has to be found between angular and energy resolution, multiplicity determination, Doppler shift and broadening.

2. Energy deposit per cell

A proper reconstruction would greatly profit from any observable carrying information on the incident direction. To investigate this point, the energy deposit in the cell which the incident direction points to as well as in a couple of surrounding cells is displayed for various photon energies in Fig.41. A 15×15 segmentation along $(\cos\vartheta, \phi)$ is considered. At low energy (1st row), nearly all particles deposit their whole amount of energy in the cell defined by the

incident direction. With increasing energy, Compton scattering in the surrounding cells is observed (2nd and 3rd rows). Above a couple of MeV (last 3 rows), escape of annihilation photon(s) from one cell to its neighbour(s) takes place as well. With increasing energy, scattering of secondary either charged particles or photons between the inner and outer shell additionally enters into play.

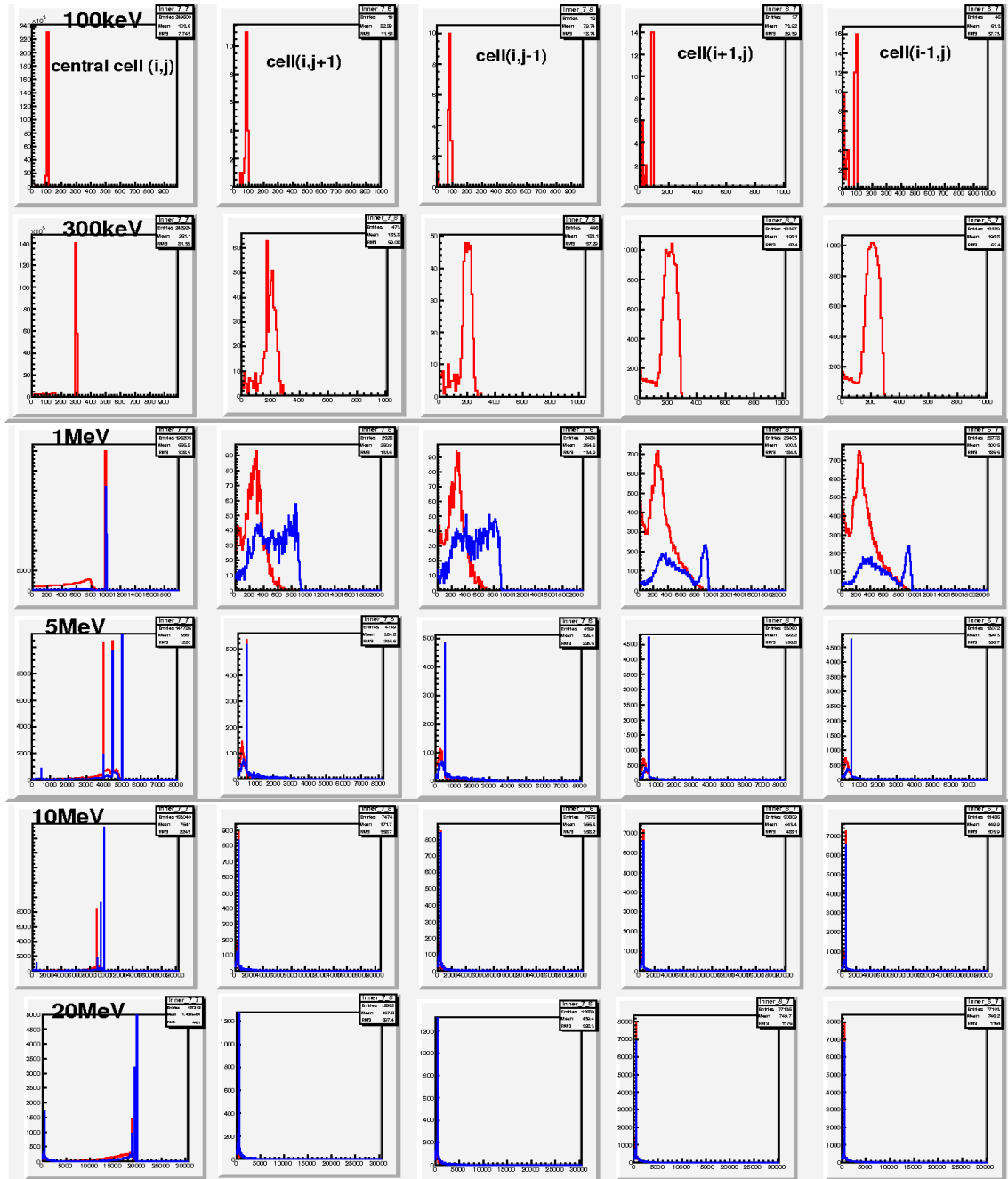


Fig. 41: Energy deposit (in keV) in a given cell around the central one defined as the cell which the incident photon points to. The 1st column corresponds to the central cell and the last 4 columns to its surrounding cells. The different rows refer to different incident energies as indicated. Red (blue) histograms correspond to the inner (outer) layer. A 15 \times 15 segmentation along $(\cos\vartheta, \phi)$ is considered. For sake of comparison, for a given incident energy (a given row), the x-same scale is chosen for the different cells (different columns).

In experiment, neither the number of incident particles, nor their emission angle are known. A relevant criterion has thus to be found which permits, starting from the measured energy deposit pattern in the whole array, to discriminate the deposits belonging to different incoming particles. According to Fig.41, for the specific segmentation considered there, in most cases, the largest amount of energy is deposited in the cell which the incoming particle points to, and the remaining part of E_{inc} is lost in the neighbouring cells. In [1] energy-weighted angular patterns already indicated that great part of the energy deposit occurs rather close to the first interaction point. We might use this property for constructing energy deposit ‘clusters’ in order to discriminate between signals caused by different particles. The cell with the largest energy deposit might constitute a relevant criterion for defining a cluster and, thus, one particle. To assess this proposition, Fig.42 shows the energy deposited in the cell which the incoming particle points to, for the inner and outer layer and several incident energies. The same information is contained in Fig.43 but displaying the percentage of energy deposited in the cell wrt to the incident energy, rather than absolute energy values. Fig.44 is similar to Fig.43 for a linear y-scale. It is observed that, whatever the final outcome of the shower generated by a particle (i.e. fully absorbed or not), the cell related to the incident direction is characterized by the largest energy deposit. Events which loss E_{inc} , ($E_{inc}-511\text{keV}$), ($E_{inc}-1022\text{keV}$), or in general more than 80% of E_{inc} , in this cell are predominant.

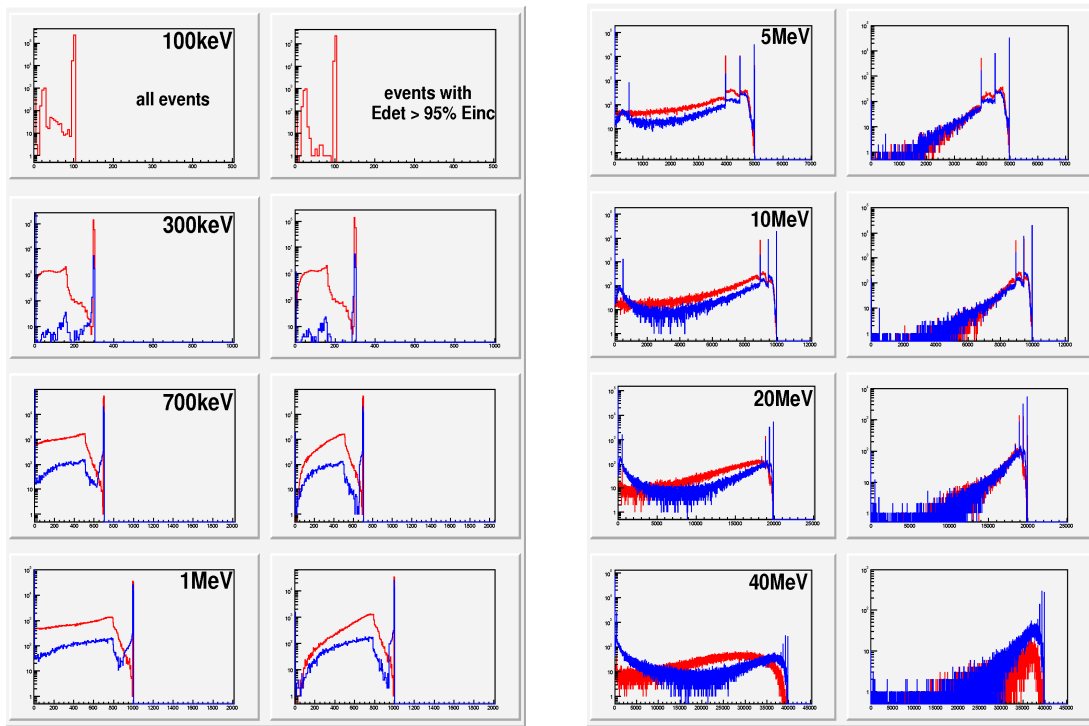


Fig. 42: Energy deposit (in keV) in the cell which the incident particle points to (cell (7,7) presently), for the inner (red) and outer (blue) layers and various incident energies. All events are included in the left columns while only fully absorbed events (with $E_{det} > 95\%$ of E_{inc}) are considered in the right ones.

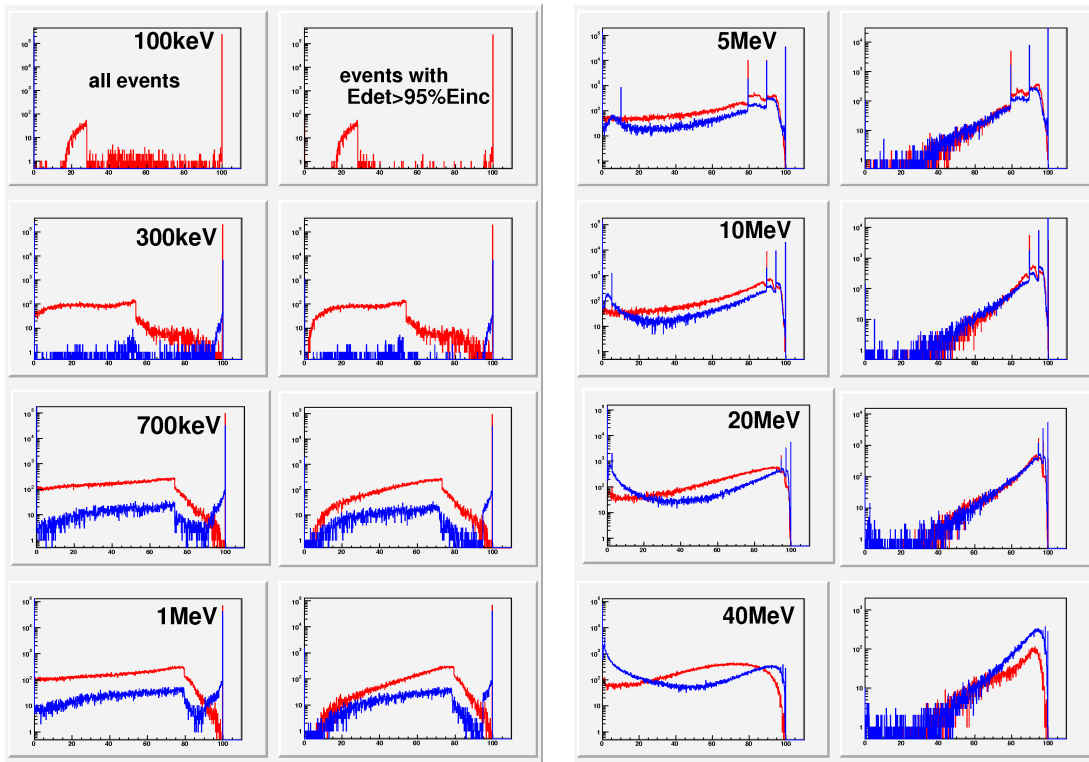


Fig. 43: Identical to Fig.42 but in terms of percentage of energy deposit wrt to E_{inc} .

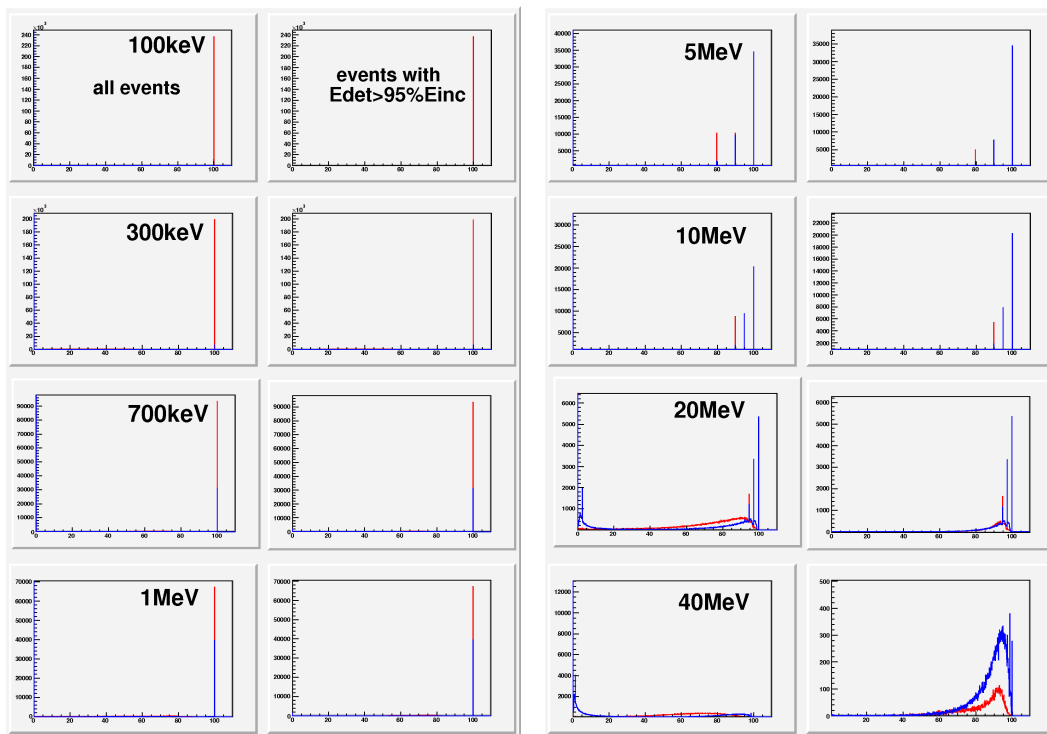


Fig. 44: Identical to Fig.43 in linear scale.

According to above, cells with large energy deposits constitute a relevant criterion for packing the collected set of signals into clusters, at least up to a few tens of MeV. Each cluster would then define one particle. The cells with maximum energy deposit can be thought as corresponding to the centre of the cluster and define the first interaction point and, hence, the direction of the incoming particle. Besides facilitating proper energy determination (via correct Doppler corrections), such a clustering procedure is also of help for the determination of the actual multiplicity. Note that the influence of packing – or not – signals does not affect much the photon energy sum (except via the Doppler correction).

The question to be raised then is the following: how to isolate and define clusters in the three-dimensional space from the signals collected over the whole array in a *a priori* two-dimensional space ? To investigate this point, we propose ordering energy deposit according to the quantity “ $o = i \cdot [\text{maximum number of cells along } \phi] + j$ “ where i and j are the indexes of the cell related to the energy signal in ϑ and ϕ direction, respectively. Fig.45 shows the distribution of the o quantity weighted by the energy deposit in the (i,j) cell. Various configurations for the incident energy and absorption are considered (see the caption). In a first stage, we consider the inner and outer layer, separately. Later on, the information from both shells might be combined in order to get some insight into the third dimension. The successive strong peaks in Fig.45-46 correspond to successive cells along the ϑ direction. In between these, each bin corresponds to different cells along the ϕ direction. For instance, for a 15×15 segmentation and an incident direction along $(90^\circ, 0^\circ)$ as presently, with $(i_0, j_0) = (7, 7)$ the cell which the incident particle points to, the central strongest peak corresponds to the combination (i_0, j_0) for which $o = 112 = 7 \cdot 15 + 7$. Its left and right next most intense side-peaks refer to the $(i_0 - 1, j_0)$ and $(i_0 + 1, j_0)$ cells, respectively. Between (i_0, j_0) and $(i_0 + 1, j_0)$ the less intense peaks are related to the cells $(i_0, j_0 + 1)$ up to $(i_0, j_0 + 14)$. The shape of the o distribution indicates that this quantity might indeed be a relevant observable: scanning the available o phase space should allow to construct and pack interaction points into clusters by looking for local maxima.

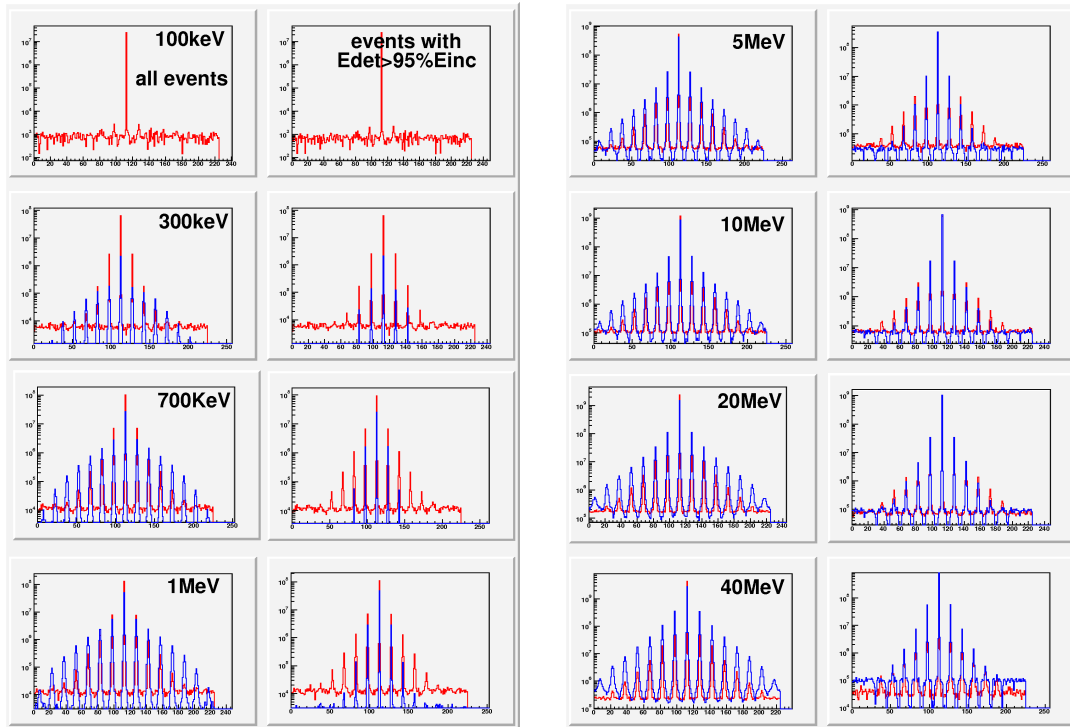


Fig. 45: Distribution of the quantity $o = i \cdot [\text{maximum number of cells along }] + j$, for the inner (red) and outer (blue) layers and various incident energies. All events are included in the left columns while only fully absorbed events (with $E_{\text{det}} > 95\%$ of E_{inc}) are considered in the right ones.

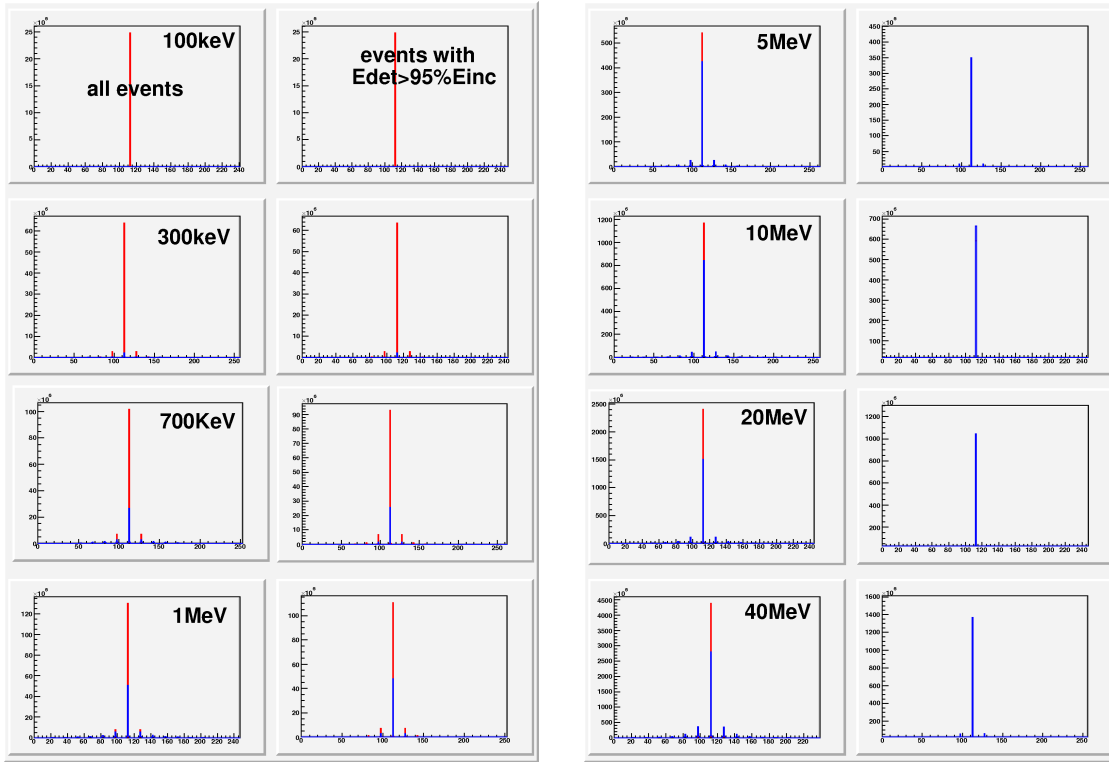


Fig. 46: Identical to Fig.45 in linear scale.

The limits of the above proposed method for constructing clustering depend on the number of photons emitted in a given event (multiplicity) and their angular distribution. We postpone the detail of such a study to forthcoming reports, but some feeling can already be obtained from Fig.47-49 where simple γ cascades with various incident energies and directions have been considered. In addition, since so far the incident photon points exactly at one point of a cell, a simulation assuming an uniform distribution of the incident particle over the cell is considered in Fig.50 for $E_{\gamma}=10\text{MeV}$: The influence on o can be noticeable (the fold might increase by up to 1 unit).

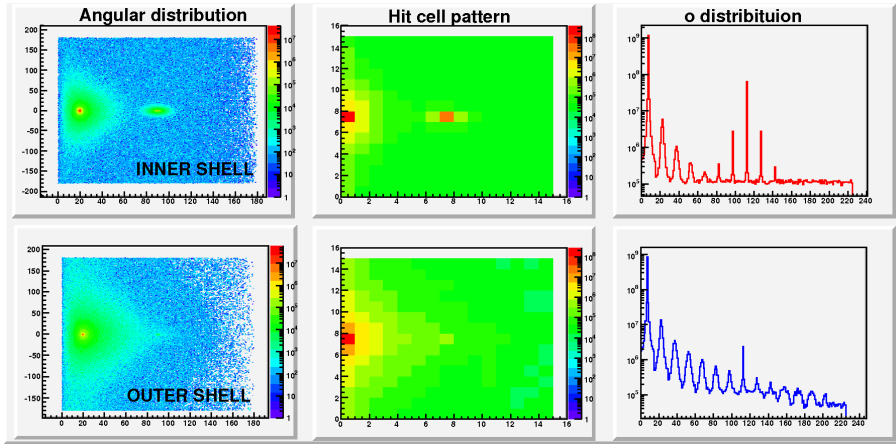


Fig. 47: Left most column: angular distribution of the incident photons. Central column: corresponding hit cell pattern. Right most column: distribution of $o = i$ [maximum number of cells along] + j . The 1st and 2nd row corresponds, respectively, to the inner and outer layers. Two incident photons are shoot: $E_\gamma=300\text{keV}$ at $(90^\circ, 0^\circ)$ and $E_\gamma=10\text{MeV}$ at $(20^\circ, 0^\circ)$. All events are included in the spectra, no condition on full absorption.

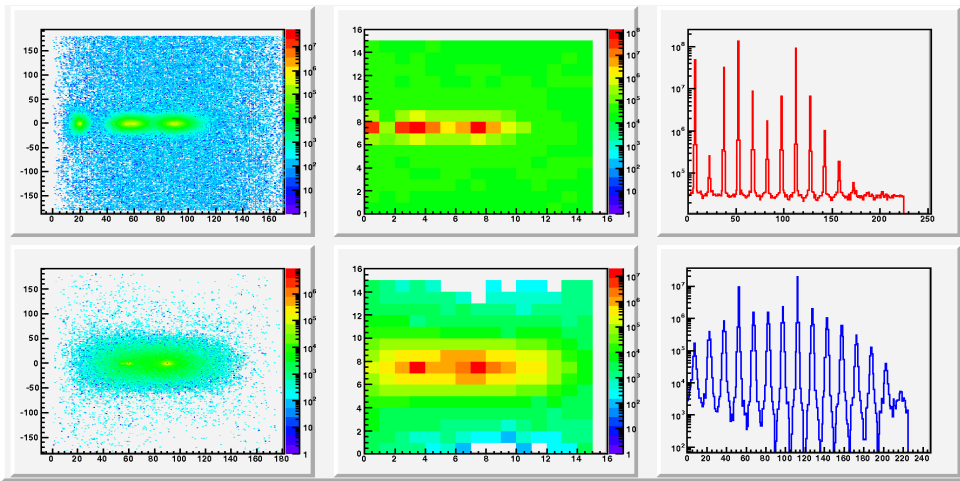


Fig. 48: Identical to the panels of Fig.47 for a cascade of five low-energy γ 's pointing at various directions: $E_\gamma=100\text{keV}$ at $(45^\circ, 0^\circ)$, $E_\gamma=200\text{keV}$ at $(20^\circ, 0^\circ)$, $E_\gamma=300\text{keV}$ at $(55^\circ, 0^\circ)$, $E_\gamma=400\text{keV}$ at $(60^\circ, 0^\circ)$ and $E_\gamma=600\text{keV}$ at $(90^\circ, 0^\circ)$. ϕ is always set at 0° .

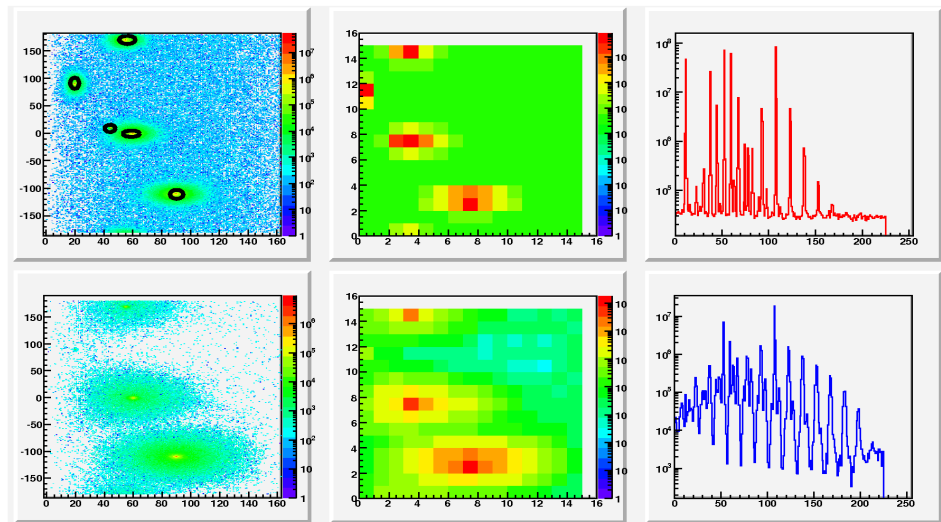


Fig. 49: Identical to the panels of Fig.48 varying the ϕ angle as well: $E_\gamma=100\text{keV}$ at $(45^\circ,10^\circ)$, $E_\gamma=200\text{keV}$ at $(20^\circ,90^\circ)$, $E_\gamma=300\text{keV}$ at $(55^\circ,170^\circ)$, $E_\gamma=400\text{keV}$ at $(60^\circ,0^\circ)$ and $E_\gamma=600\text{keV}$ at $(90^\circ,250^\circ)$. The directions of the 5 incident particles are materialized by thick contours in the upper left most picture.

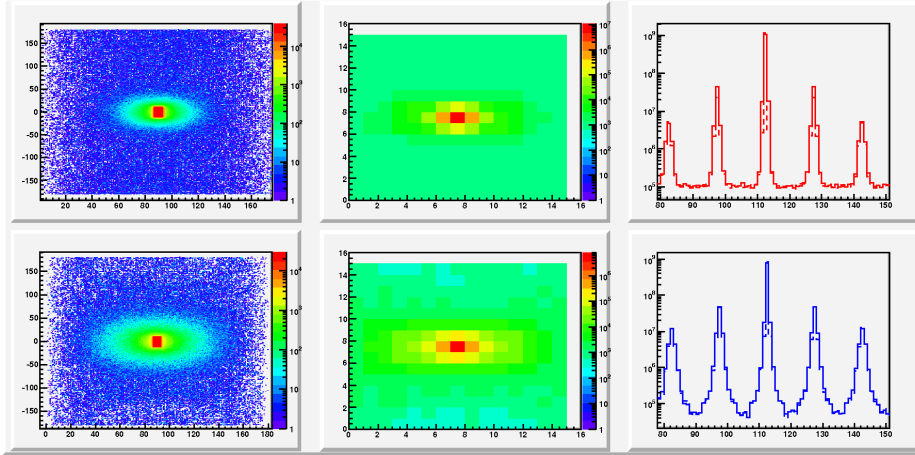


Fig. 50: Identical to the panels of Fig.47 for a single incident photon with $E_\gamma=10\text{MeV}$ uniformly shoot in the cell centred around $(90^\circ,0^\circ)$ instead of an incident direction pointing at the centre of the cell exactly. For the last columns, full lines represent the distribution for an uniform angular distribution over the central cell, while the dashed histograms corresponds to photons pointing exactly at $(90^\circ,0^\circ)$.

According to above, at very high multiplicity the discrimination power of o dramatically decreases, if helpful at all. Yet, combining the information of the two layers might allow going further in resolving different particles, and further informing about the third (in depth) direction. Hence, we might look at correlations between the inner vs. the outer shell. This shall permit determining whether cells fired in one event in the inner and outer layer stem from the same particle and, thus, have to belong to the same cluster. Such correlations will be done together with the investigation of reconstruction algorithms in the forthcoming studies.

3. Attempts of add-backs and efficiency

3.1. Efficiency per cell

Segmentation brings crucial information on the angle of the γ -ray, what is namely mandatory for proper Doppler correction and angular distribution/correlation studies. At the same time, it complicates the determination of the true number of emitted γ 's; in general, the fold (measured number of fired cells) does reflect the multiplicity (number of photons indeed emitted in a given event). In the same line, the determination of the energy of the photon fully relies on the reconstruction procedure used i.e. on the knowledge of the cells to be added-back. In [1] we have discussed the efficiency of *un-segmented* shells, or equivalently made of a single segment, and defined efficiency in terms of probability for full absorption in a given shell i.e. a given single segment. Below, we consider the opposite extreme case, assuming that each fired cell in one event corresponds to one photon. That is equivalent to exclude scattering between cells, and means *no* add-back at all. The efficiency thus corresponds to the probability of fully absorbing the incident γ in ONE cell. This efficiency is displayed as function of E_{inc} for the inner and outer cells in Fig.51 for various segmentation configurations and an incident direction along $(90^\circ,0^\circ)$. Unsurprisingly, the larger the number of segments, the lower the efficiency per segment; with the effect increasing with increasing energy. It is to

be noted that the segmentation along $\cos\vartheta$ seems to govern the efficiency: there is almost no difference for either 9 or 15 cells in ϕ . For sake of comparison, we remind in Fig.52 the absorption curves obtained in [1] without segmentation. The loss of efficiency introduced by segmentation and without applying any add-back is, of course, most critical above a few MeV with increasing extension of the shower generated by the incident photon. Besides, the corresponding multiplicity being equal to the fold in that case is, of course, highly un-correct.

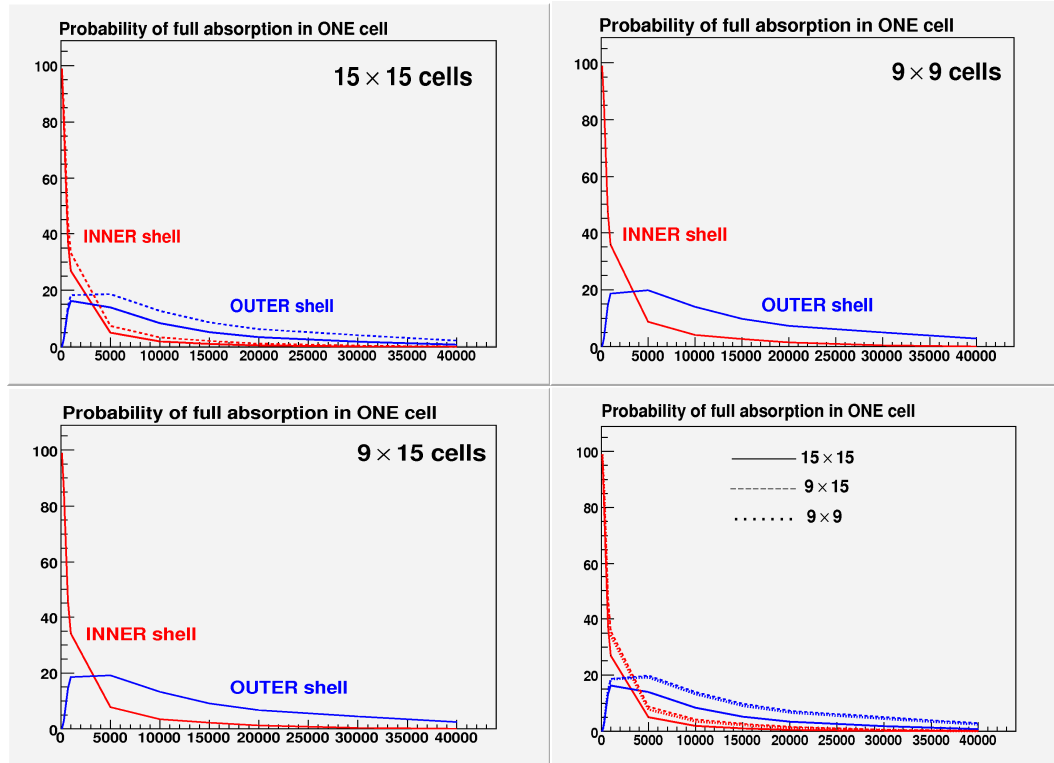


Fig. 51: Probability of fully absorbing the incident photon in one cell of either the inner (red) or the outer (blue) shell. Full absorption is defined as $E_{det} > 98\%$ of E_{inc} (cf. [1]). The upper-left panel corresponds to a 15×15 segmentation along $(\cos\vartheta, \phi)$ (full lines) or along (ϑ, ϕ) (dashed lines). The upper-right and lower-left panels refer to a 9×9 and 9×15 segmentation, respectively, with uniform cutting along $(\cos\vartheta, \phi)$ in both cases. The lower-right panel superimposes the curves related to a $(\cos\vartheta, \phi)$ segmentation with different numbers of segments.

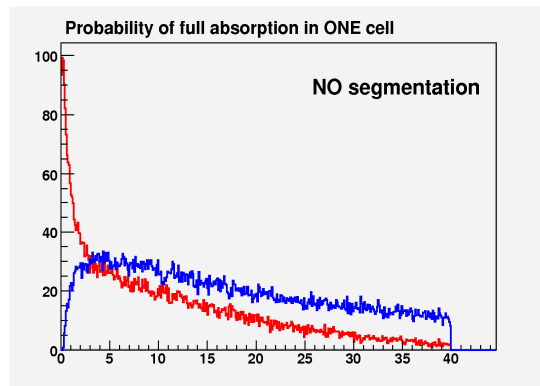


Fig. 52: Probability of fully absorbing the incident photon in either the inner (red) or the outer (blue) shell [1].

The dependence of the efficiency on the direction of the incoming particle is illustrated in Fig.53. Except for very small angles (not shown and anyway ‘out of reach’ experimentally), the efficiency does not depend strongly on the initial γ -ray direction for a 15×15 segmentation along $(\cos\vartheta, \phi)$. This is not surprising and could already be inferred from Fig.38 where the corresponding fold distributions are very similar. This is related to the fact that the energy deposit is concentrated around a rather narrow cone around the first interaction point. Yet, we emphasize that the same conclusion does *not* necessarily hold for the reconstruction algorithm. On the contrary, according to above, the latter might strongly depend on the initial direction depending on the segmentation adopted for the complete device. Along the remainder of this work, unless explicitly specified, the direction of the incident particle is set at $(90^\circ, 0^\circ)$.

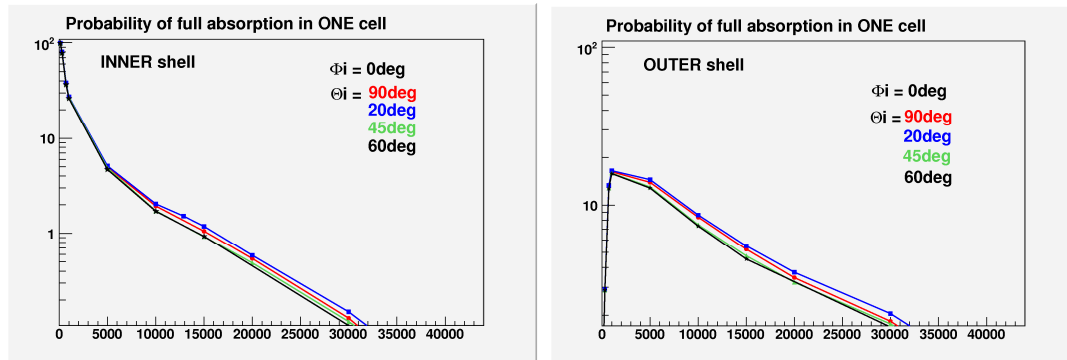


Fig. 53: Probability of fully absorbing the incident photon in one cell of either the inner (left) or the outer (right) shell. A 15×15 segmentation along $(\cos\vartheta, \phi)$ is considered and various directions for the incoming particle as indicated.

Note that the full absorption criterion considered in the above discussed pictures is $E_{\text{det}} > 98\%$ of E_{inc} , what is rather severe. For practical cases, the efficiency might thus be slightly more optimistic than what displayed in Fig.51-53.

3.2. Simplest add-back procedures

Further, we propose packing the cells according to 3 ‘crowns’ as illustrated in Fig.54. The percentage of energy deposit in each of these packs is shown in Fig.55 for the inner and outer shell for different incident energies. From there, it is obvious that, with increasing incident energy, including more and more cells in the add-back procedure - by enlarging the crown around the incident direction - permits restoring a greater amount of energy. Although the full-energy peak profits from adding more cells back, the tail of the peak grows as well. Furthermore, quite surprisingly the two-photon annihilation peak becomes also more intense. Fig.56 shows a zoom on the full-energy peak and the 1022keV peak for one example. To investigate these observation further, we display in Fig.57 the same spectra as in Fig.55 but including only those events which are fully absorbed (with the criterion of $E_{\text{det}} > 95\%$ of E_{inc}) in either the inner or the outer shell. It is clearly observed there that increasing the number of cells added-back increases only the full-energy peak while the tail is reduced. The peaks related to the escape of one and two annihilation photon(s) from the largest crown are on average one up to two orders of magnitude smaller than the full-energy peak. Note that the gain in restoring the true energy is larger from crown2 \rightarrow crown3 as compared to

crown1 \rightarrow crown2. As an example, for $E_{inc}=10\text{MeV}$, the full-energy peak increases by about 25% from crown1 \rightarrow crown2 and by nearly 60% from crown1 \rightarrow crown3. This gain is directly dependent on the spatial extension of the shower generated the incident photon and therefore on E_{inc} . In [1] we have seen that, in most critical cases of multiple-scattering, the shower hardly extends beyond $\pm 15^\circ$ ($\sim 200\text{msr}$) around the incident direction. For the segmentation considered presently, this range is somewhere in between crowns 2 and 3 (see Table 2 in Appendix A) (depends essentially on the segmentation in the ϑ direction, the segments along ϕ being large).

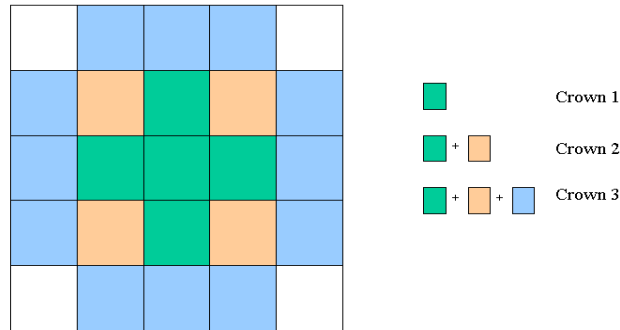
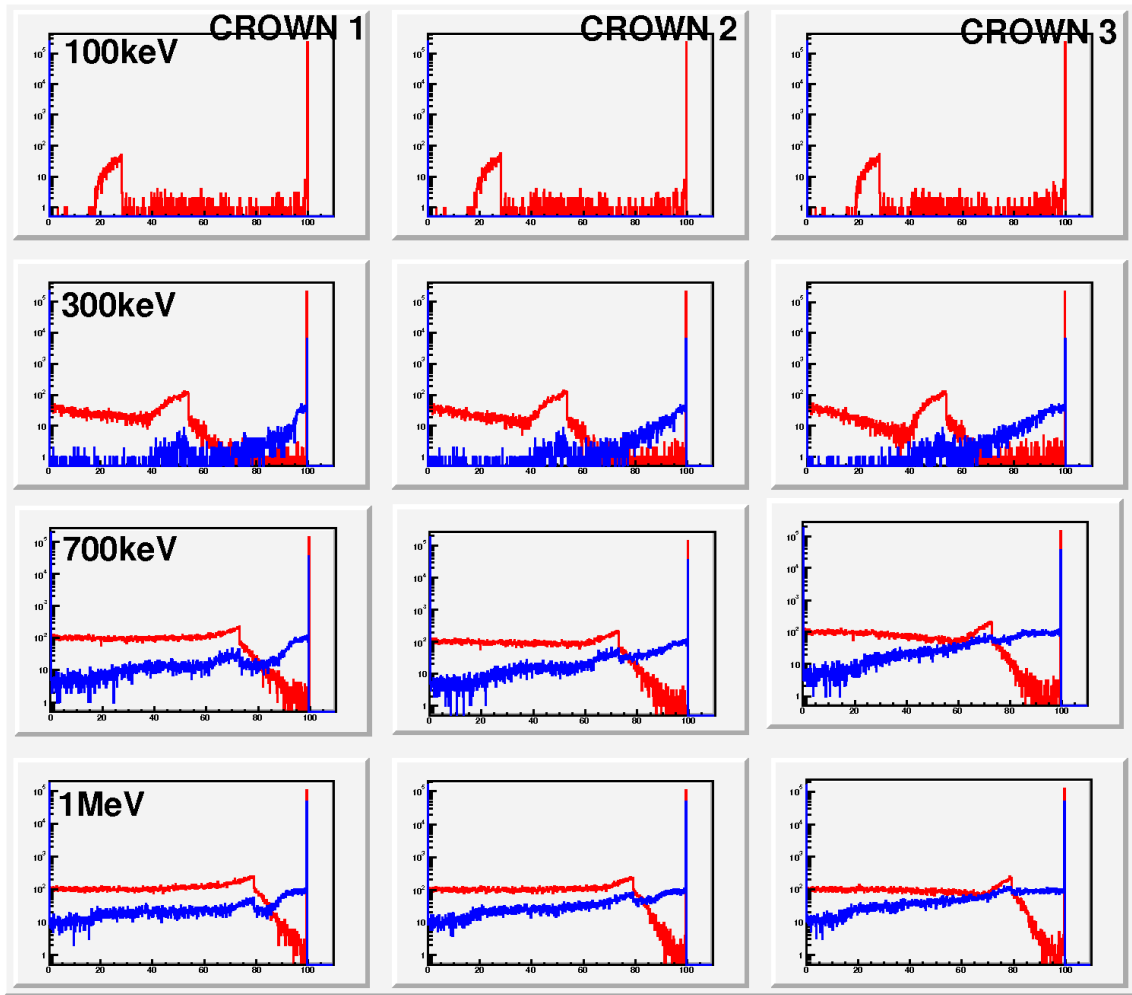


Fig. 54: Schemes of the ‘packs’ used for adding energies back, see the text.



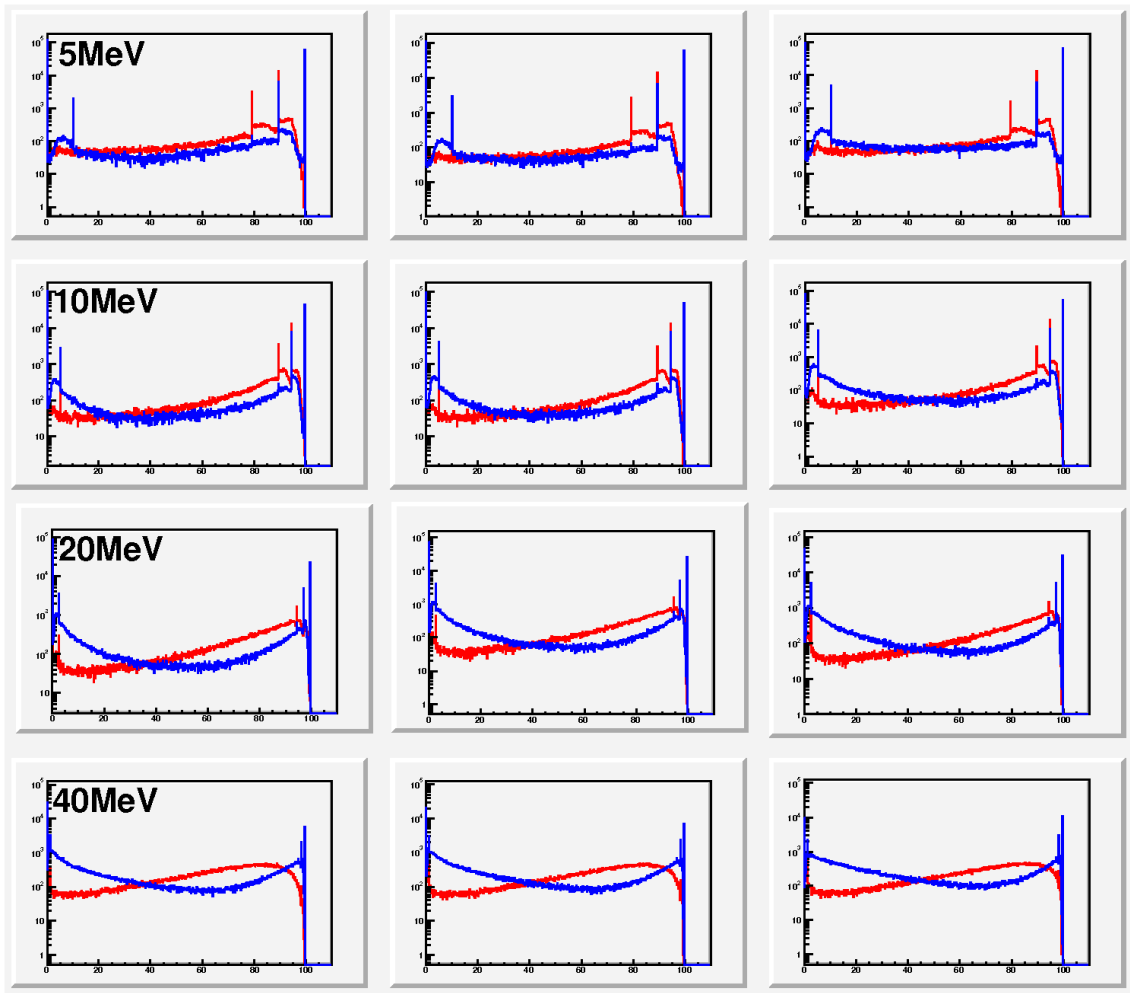


Fig. 55: Percentage of energy deposit wrt the incident energy in inner (red) and outer (blue) shell. Each row refers to another incident energy as indicated. The different columns correspond to 3 different ways of ‘packing’ neighbouring cells together as defined in the text and Fig.54.

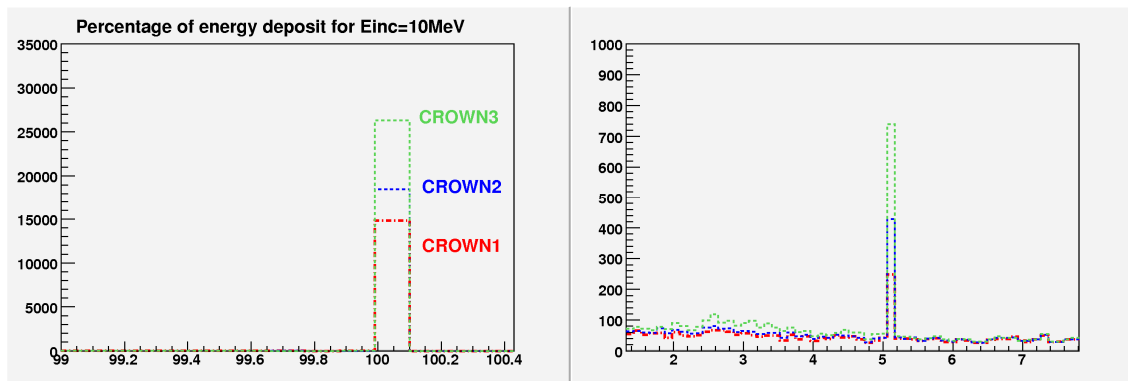


Fig. 56: Zoom on the spectra of Fig.45 for $E_{inc}=10\text{MeV}$ for the inner shell around the full-energy peak which corresponds to 100% of E_{inc} absorbed (left) and the peak at 511keV which corresponds to about 5% of E_{inc} absorbed (right). The various colours refer to different add-back procedures: crown 1 (dashed red), crown 2 (dashed blue) and crown 3 (dashed green).

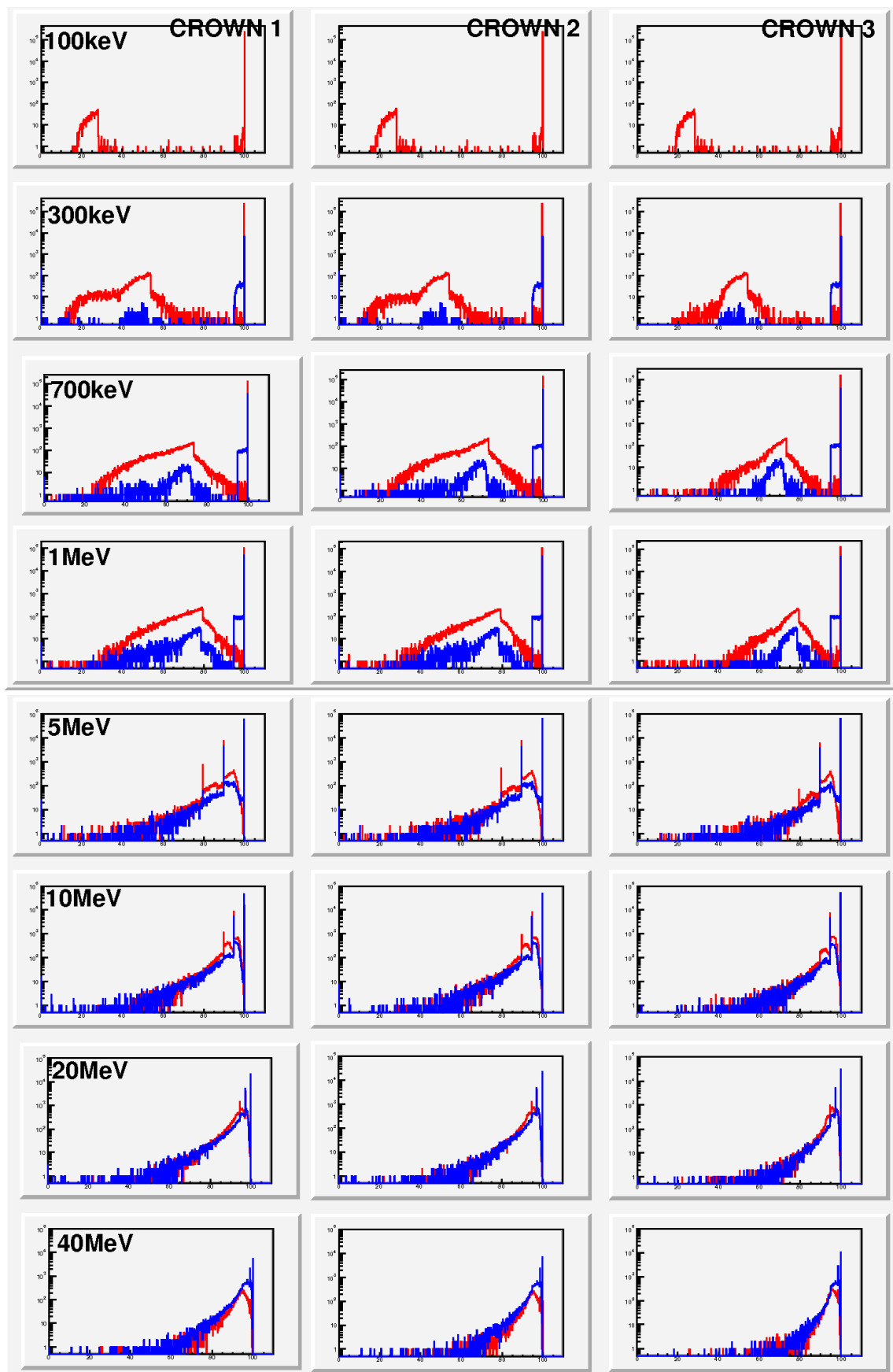


Fig. 57: Similar to Fig.55 but only with those photons which are fully absorbed in either the inner (red) or the outer (layer). See the text.

The number of events which deposit more than 50% and 90% of E_{inc} in the various crowns in a given shell is shown as a function of E_{inc} on Fig.58 and 59, respectively. The observed weak dependence on the size of the crown suggests that of energy deposit occur very close to the incident cell even for the highest E_{inc} : More than 50% of the events deposit more than 50% of E_{inc} in the incident cell and its 4 adjacent neighbours. Remind that for interpreting the result for the outer shell we shall keep in mind that it depends on what occurs in the inner layer (the incoming flux differs for the two shells). Hence, the dip at low-energy in the outer shell is caused by the fact that all such photons lose most of the energy already in the inner shell. At high energy, the behaviour is similar to that in the inner shell since for the greatest part of those events which deposit energy in the inner shell deposit there more than 50% of E_{inc} , so that they do not contribute to the outer shell histogram.

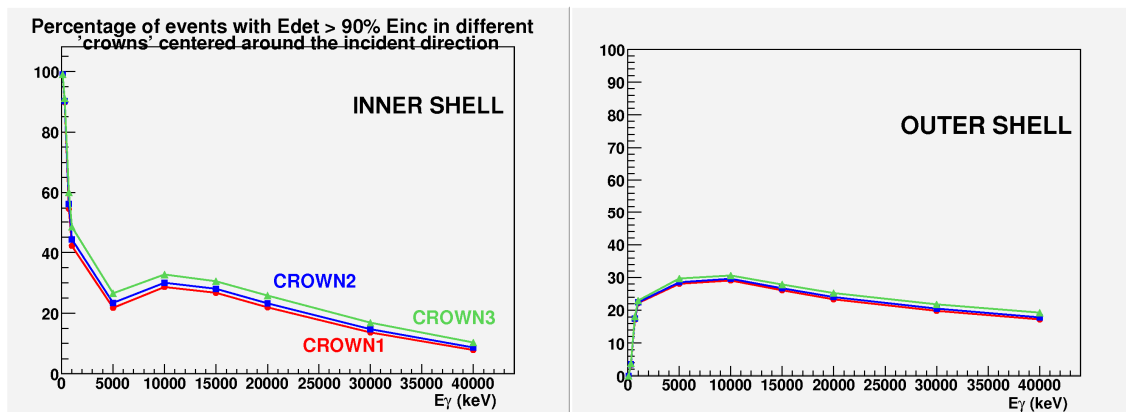


Fig. 58: Number of events depositing more than 90% of E_{inc} in a given crown in the inner (left) and outer (right) shell. The different colours refer to the above-defined 3 crowns as indicated.

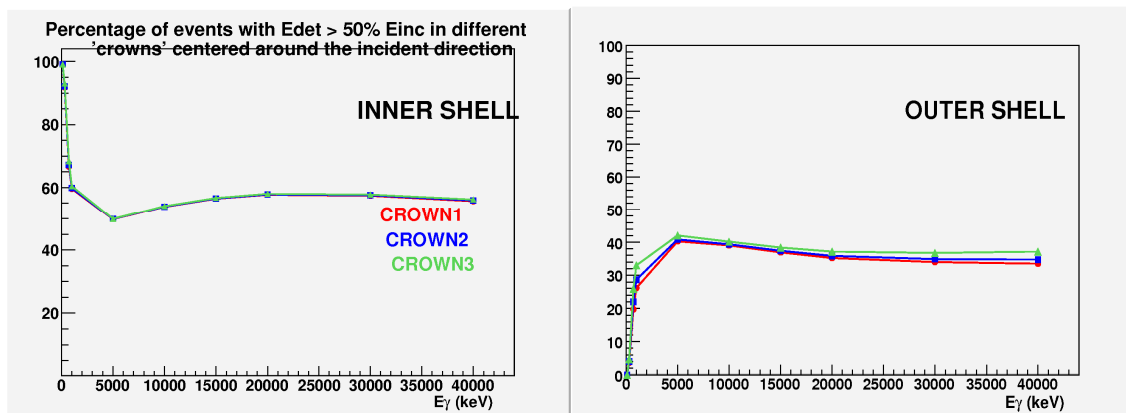


Fig. 59: Number of events depositing more than 50% of E_{inc} in a given crown in the inner (left) and outer (right) shell. The different colours refer to the above-defined 3 crowns as indicated.

Appendix A

The angles ϑ and ϕ delimiting the segmentation of a full spherical shell into 15×15 cells distributed uniformly along ϑ and ϕ and $\cos\vartheta$ and ϕ are given tables 1 and 2, respectively. In both cases, $\vartheta=0$ and $\phi=0$ are chosen for the origin of cell numbering i and j . For the latter segmentation option, the value of $\cos\vartheta$ is indicated as well.

Cell	ϑ_{\min}	ϑ_{\max}	ϕ_{\min}	ϕ_{\max}
0	0	12	-180	-156
1	12	24	-156	-132
2	24	36	-132	-108
3	36	48	-108	-84
4	48	60	-84	-60
5	60	72	-60	-36
6	72	84	-36	-12
7	84	96	-12	+12
8	96	108	+12	+36
9	108	120	+36	+60
10	120	132	+60	+84
11	132	144	+84	+108
12	144	156	+108	+132
13	156	168	+132	+156
14	168	180	+156	+180

Table 1: Angles defining the limits of the cells for a uniform segmentation of the array in 15×15 cells along the ϑ and ϕ directions (leading to $\Delta\vartheta=12^\circ$ and $\Delta\phi=24^\circ$). For practical reason, we decide numbering cells at 0.

Cell	$\cos\vartheta_{\min}$	$\cos\vartheta_{\max}$	ϑ_{\min}	ϑ_{\max}	ϕ_{\min}	ϕ_{\max}
0	1	0.8666	0	29.93	-180	-156
1	0.8666	0.7333	29.93	42.833	-156	-132
2	0.7333	0.6	42.8333	53.13	-132	-108
3	0.6	0.4666	53.13	62.18	-108	-84
4	0.4666	0.3333	62.18	70.52	-84	-60
5	0.3333	0.2	70.52	78.46	-60	-36
6	0.2	0.0666	78.46	86.177	-36	-12
7	0.0666	-0.0666	86.117	93.82	-12	+12
8	-0.0666	-0.2	93.82	101.54	+12	+36
9	-0.2	-0.3333	101.54	109.47	+36	+60
10	-0.3333	-0.4666	109.47	117.82	+60	+84
11	-0.4666	-0.6	117.82	126.87	+84	+108
12	-0.6	-0.7333	126.87	137.167	+108	+132
13	-0.7333	-0.8666	137.167	150.07	+132	+156
14	-0.8666	-1	150.07	180	+156	+180

Table 2: Angles defining the limits of the cells for a uniform segmentation of the array in 15×15 cells along the $\cos\vartheta$ and ϕ directions (leading to $\Delta\cos\vartheta=0.1333$ and $\Delta\phi=24^\circ$). For practical reason, we decide numbering cells at 0.

-
- [1] Report 1 on the PARIS Calorimeter Simulations (<http://nz22-13.ifj.edu.pl/~myalski/paris/news.php?lng=en>).
- [2] Report 2 on the PARIS Calorimeter Simulations.